Draft version September 23, 2026
Typeset using LaTeX **twocolumn** style in AASTeX7.0.1

The δ Scuti instability strip and period–luminosity relation as seen by TESS and Gaia DR3

Daniel Hey [1], Simon Murphy [2], Timothy R. Bedding [3], Anuj Gautam [2], Daniel Huber [1], Yaguang Li [1], Ian Berry [1], Hyde Kenney [4,1], Prasad Mani [3], Tom Love [2], and Mykyta Kliapets [5]

[1] Institute for Astronomy, University of Hawaiʻi, 2680 Woodlawn Drive, Honolulu, HI 96822, USA
[2] Centre for Astrophysics, University of Southern Queensland, Toowoomba, QLD 4350, Australia
[3] Sydney Institute for Astronomy, School of Physics, University of Sydney, NSW 2006, Australia
[4] Department of Astronomy, University of Florida, Gainesville, FL 32611, USA
[5] Institute of Astronomy, KU Leuven, Celestijnenlaan 200D, bus 2401, 3001 Leuven, Belgium

ABSTRACT

We present an asteroseismic survey of 1,526,218 A- and F-type stars in and around the δ Sct instability strip using TESS 10-minute cadence data. The fast sampling allows, for the first time, to resolve the full δ Sct pulsation spectra for stars spanning nearly the entire sky. We derive homogeneous stellar parameters by combining *Gaia* DR3 parallaxes and archival photometry, and we validate the resulting temperature scale against interferometry, finding temperature agreement to within ∼300 K. We classify δ Sct pulsators using a Positive–Unlabelled learning framework, identifying 156,706 pulsators with detection classification greater than 0.9. From this, we confirm that δ Sct stars are, on average, significantly faster rotators than their non-variable A-type counterparts. We map the observational instability strip in the $T_{\rm eff}$–$\log L$ plane and confirm that the classical strip is not pure: the pulsator fraction peaks at ∼ 30% over the full sample and rises to ∼ 80% in the brightest magnitude bins, demonstrating that detection sensitivity accounts for much, but not all, of the apparent impurity. We refine the δ Sct period–luminosity relation using our *Gaia* DR3 luminosities and find results consistent with previous determinations, and recast it as a scale-invariant period–density relation that connects directly to the pulsation constant. From this, we infer that the secondary ridge in the relations is probably a combination of several overtone modes. We further show that δ Sct variables lying closest to the fundamental ridge have systematically lower rotational velocities, and occupy a distinct region of the observed instability strip. Finally, by cross-matching against a *Gaia* catalog of open clusters, we demonstrate a correlation between the mean pulsation frequency of δ Sct stars and cluster age, suggesting a new ensemble asteroseismic age indicator for young stellar populations.

Keywords: Asteroseismology (73) — Stellar oscillations (1617) — Delta Scuti variable stars (370) — Stellar astronomy (1583)

1. INTRODUCTION

The δ Scuti variables are intermediate-mass (1.5–2.3 $M_\odot$) main-sequence stars located within the classical instability strip (M. Breger 1979, 2000; K. Uytterhoeven et al. 2011). They exhibit low radial-order pressure (p) modes driven primarily by the κ mechanism believed to be acting in the second helium ionisation zone, with pulsation frequencies typically spanning 5–70 $\rm d^{-1}$ and effective temperatures in the range 6500–10 000 K (G. Houdek 2000; V. Antoci et al. 2019; D. Kurtz 2022). As intermediate-mass main-sequence pulsators, the δ Sct stars are progenitors of the bulk of the white-dwarf mass distribution (J. D. Cummings et al. 2018) and provide an important link between the well-studied solar-like oscillators and the more massive β Cephei and slowly pulsating B stars.

Email: dhey@hawaii.edu

Despite their potential as asteroseismic probes, the δ Sct stars have long resisted systematic mode identification routinely applied to the solar-like oscillators. In stars cooler than the Kraft break (R. P. Kraft 1967; A. C. Beyer & R. J. White 2024), stochastic excitation by near-surface convection drives (and damps) the full range of modes within a resonant envelope, producing the regular comb of frequencies used for solar-like asteroseismology (e.g. W. J. Chaplin et al. 2011). Pulsations in δ Sct stars, by contrast, are driven by a heat-engine mechanism and only an apparently pseudo-random subset of modes are excited across much wider frequency ranges. Their mode selection mechanism thus remains poorly understood (M. Breger et al. 2009; D. M. Bowman & D. W. Kurtz 2018).

Mode identification is further complicated by the rapid rotation typical of A-type stars (J. Zorec & F. Royer 2012), which lifts the degeneracy of azimuthal mode components and produces dense, asymmetric splitting (C. Aerts et al. 2010; C. Aerts & A. Tkachenko 2024; Z. Guo et al. 2024). Only with the high-cadence, all-sky coverage of the Transiting Exoplanet Survey Satellite (TESS; G. R. Ricker et al. 2015) mission h as a subset of so-called "nice" δ Sct variables been identified that show regular, identifiable modes with a clear frequency spacing ($\Delta\nu$) that is a good diagnostic of stellar density (T. R. Bedding et al. 2020). These targets usually lie close to the zero-age main sequence and pulsate at high frequencies (≥ 40 d^{-1}), and they have provided the first robust mode identifications in this class, marking a pathway towards the asteroseismic exploitation of the larger population of δ Sct stars with more complicated pulsation spectra.

A closely related question is whether all stars within the δ Sct instability strip pulsate and, if not, what mechanisms distinguish the pulsators from their quiescent counterparts. It is now well established, largely through the *Kepler* mission, that the instability strip is not pure: even after accounting for the reduced detection sensitivity at fainter magnitudes, the pulsator fraction peaks at only ∼70% at the centre of the observational strip (S. J. Murphy et al. 2019), and around half of the stars in the δ Sct temperature range show no detectable pulsation (L. A. Balona & W. A. Dziembowski 2011; L. A. Balona et al. 2015). Conversely, a small population of δ Sct variables has recently been identified lying outside the classical strip (K. Thomson-Paressant et al. 2025), blurring its boundaries in the opposite sense. A limitation of the large *Kepler* population studies was that most A/F targets were observed at 30-minute cadence, placing the nominal Nyquist frequency at $\approx 24\,\mathrm{d}^{-1}$, well below the upper end of the δ Sct pulsation range. The slightly irregular observing cadence of *Kepler*, once barycentric time corrections had been made, allowed intrinsic super-Nyquist frequencies to be distinguished from their aliases (S. J. Murphy et al. 2013; H. Shibahashi & S. J. Murphy 2018; D. R. Hey et al. 2019), although the non-zero integration times attenuated their observed amplitudes and complicated population-level selection and amplitude comparisons.

Subsequent work has highlighted the dominant role played by rotation in shaping the δ Sct population. K. Gootkin et al. (2024) classified ∼16,000 δ Sct variables using *TESS* 30-minute FFI photometry and showed that the pulsator fraction within the instability strip is a strong function of rotational velocity, traced by the *Gaia* `vbroad` line-broadening parameter. S. J. Murphy et al. (2024a) and J. Wang et al. (2025) reached a similar conclusion using independent data. Recently, I. Berry et al. (2026) further suggest a correlated age dependence. These findings are consistent with the expectation that the partial ionisation zone responsible for the κ mechanism is more efficiently maintained against gravitational settling in rapidly rotating stars, providing an explanation for the lower pulsator fraction among the slowly rotating, chemically peculiar Am stars (M. Breger 1979; D. W. Kurtz et al. 1989; O. Dürfeldt-Pedros et al. 2024). However, the existence of a small population of slowly-rotating δ Sct pulsators within the instability strip remains poorly understood, pointing towards an alternative excitation mechanism such as the turbulent pressure invoked by V. Antoci et al. (2014).

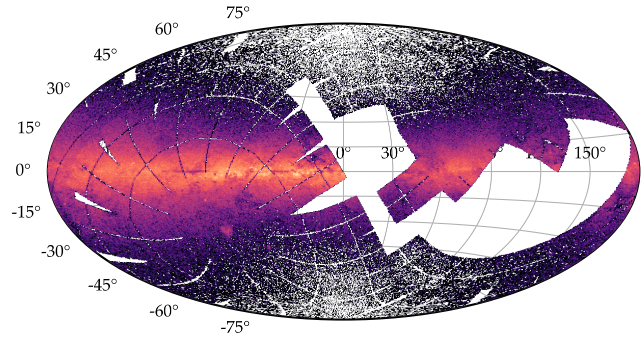

Figure 1. Sky distribution of the A/F sample (Section 2.1) in Galactic coordinates, colored by the density of points. Note the dearth of targets in certain regions caused by the absence of TESS pointings in Sectors 27 through 55 used in this study.

The *TESS* mission now provides the data needed to address these questions on a homogeneous basis. The 10-minute FFI cadence available from *TESS* Cycle 3 (Sector 27) onwards (J. M. Jenkins et al. 2021) places the Nyquist frequency at $72\,\mathrm{d}^{-1}$, bringing most of the δ Sct pulsation range below the nominal Nyquist limit and substantially reducing the aliasing encountered in 30-minute data. Combining with the precise parallaxes and photometry of *Gaia* DR3 (G. Collaboration et al. 2023) allows us to calculate luminosities and effective temperatures for over a million A and F stars across the sky to a precision previously available only for the small *Kepler* sample.

In this paper, we combine *TESS* 10-minute FFI photometry from Sectors 27 through 55 (Cycle 3 and 4) with *Gaia* DR3 parallaxes to construct a nearly all-sky sample of 1,526,218 A- and F-type stars (Figure 1). We use this sample to characterise the δ Sct population across the HRD, investigate the period–luminosity relation, investigate the effects of rotation, and produce a catalogue of δ Sct variables in open clusters.

2. DATA

2.1. *Target selection*

We selected our targets from the *TESS* Input Catalog (TIC; K. G. Stassun et al. 2018) because of its all-sky homogeneity. We applied a temperature cut of $6300 \leq T_{\mathrm{eff}} \leq 10{,}000\,\mathrm{K}$ and a magnitude cut of

$T < 13.5$ mag. The temperature range encompasses the classical δ Sct instability strip (S. J. Murphy et al. 2019; M. A. Dupret et al. 2004) with a buffer of ∼200 K on the cool side, sufficient to capture pulsators whose catalogued temperatures are systematically biased. Stars hotter than 10,000 K are predominantly B-type pulsators (β Cep, SPB) and lie outside the scope of this work, while genuine δ Sct stars cooler than 6300 K are rare and probably result from inaccurate photometric temperatures.

We further required each target to have a *Gaia* DR3 source match with a fractional parallax uncertainty $\sigma_\pi/\pi < 0.2$, which removed 12,714 targets and ensured that distances (and hence luminosities) are well constrained. Applying these cuts yielded a parent sample of 1,526,218 A- and F-type stars, shown in Figure 1.

2.2. *TESS photometry*

We used *TESS* 10-minute full-frame image (FFI) light curves, which became available from Cycle 3 (Sector 27) onwards (G. R. Ricker et al. 2015; J. M. Jenkins et al. 2021). The 10-min cadence places the Nyquist frequency at 72 d^{-1}, bringing most of the expected δ Sct pulsation range below the nominal Nyquist limit and greatly reducing the aliasing affecting *Kepler* long-cadence studies (S. J. Murphy et al. 2013; H. Shibahashi & S. J. Murphy 2018; D. R. Hey et al. 2019) and earlier *TESS* studies based on 30-minute FFIs (K. Gootkin et al. 2024). Although shorter-cadence FFIs of 200 s are now available from Cycle 5 onwards, we restricted our work to the 10-min FFIs in Cycles 3 and 4 in order to produce a homogeneous all-sky sample.

We used light curves produced by the TGLC pipeline (TESS–Gaia Light Curve T. Han & T. D. Brandt 2023), which performs PSF photometry on the *TESS* FFIs using a forward model of the local stellar field constructed using *Gaia* DR3 as a prior. For each target, we stitched together all available 10-minute FFI sectors and applied a high-pass filter to remove instrumental systematics and long-term trends. This high-pass filtering was achieved by smoothing the light curve with a Gaussian with FWHM 1 d^{-1} and subtracting this smoothed version from the original. We utilized the internal cross-match provided in the TGLC bulk download scripts, which maps the *Gaia* DR3 IDs to a corresponding TIC ID. When this work was done, bulk downloads for the TGLC photometry were only available up to Sector 58. Because of this, we restricted our analysis to Sectors 27 through 55 inclusive, covering TESS cycles 3 and 4.

We computed the Lomb–Scargle periodogram (N. R. Lomb 1976; J. D. Scargle 1982; J. T. VanderPlas 2018) of each light curve up to the nominal Nyquist frequency of 72 d^{-1}. This provides unaliased frequency measurements for most δ Sct modes, although modes intrinsically above 72 d^{-1} remain aliased and the amplitudes of modes approaching the Nyquist limit are attenuated by the non-zero integration time.

2.3. *Gaia DR3 parallaxes and photometry*

For each target we retrieved *Gaia* DR3 parallaxes, broadband G, $G_{\rm BP}$, and $G_{\rm RP}$ photometry, and the `vbroad` line-broadening parameter where available (G. Collaboration et al. 2023). We found that 94% of our sample have $\sigma_\pi/\pi < 0.05$. We made no further selection on photometric quality but we did require that the *Gaia* DR3 `ruwe` flag was < 1.4, to exclude probable astrometric binaries whose parallaxes may be biased (L. Lindegren 2018), which excludes 16.8% of our sample. While this high RUWE sample is excluded from analysis (Sec. 5 onwards), it is still present in our final table and flagged accordingly.

The `vbroad` parameter was available for 434,987 of our targets. This provides a measure of spectral line broadening that combines contributions from rotation, micro- and macroturbulence, and unresolved binarity. While not exactly equivalent to the projected rotational velocity, `vbroad` has been shown to correlate well with $v \sin i$ for A- and F-type stars (Y. Frémat et al. 2023). We note that `vbroad` carries known temperature- and magnitude-dependent systematics and is least reliable at low broadening (Y. Frémat et al. 2023), however S. J. Murphy et al. (2024a) showed that it is moderately reliable for the A/F stars in most rotation regimes.

3. STELLAR PROPERTIES

We derived homogeneous stellar properties for our full sample using the ISOCLASSIFY package (D. Huber et al. 2017), which has been validated against asteroseismic and interferometric benchmarks for FGK stars (T. A. Berger et al. 2020, 2026). Here, we extend its use to the considerably hotter A- and early F-type regime, and verify the reliability of the stellar parameters using interferometry.

ISOCLASSIFY provides two modes of operation. In *direct* mode, effective temperatures are derived from empirical surface-brightness–color relations (L. Casagrande et al. 2010; D. Graczyk et al. 2017), and the stellar radius is then obtained directly from the angular diameter, parallax, and bolometric flux. In *grid* mode, observed quantities (parallax, apparent magnitudes, spectroscopic constraints, etc.) are compared against a grid of stellar isochrones, and posterior distributions over $T_{\rm eff}$, log g, mass, radius, and age are obtained by marginalising over the grid. The two modes are complementary: direct mode is largely model-independent and is the preferred choice for cool, well-calibrated stars, while grid mode incorporates stellar-evolution physics and performs better in regimes where the color–temperature relations are poorly calibrated.

For our sample of A- and F-type stars, direct mode is expected to perform poorly. The peak of the spectral energy distribution of an A-type star lies in the ultraviolet, so optical and near-infrared colors sample the Rayleigh–Jeans tail of the Planck function and become only weakly sensitive to effective temperature.

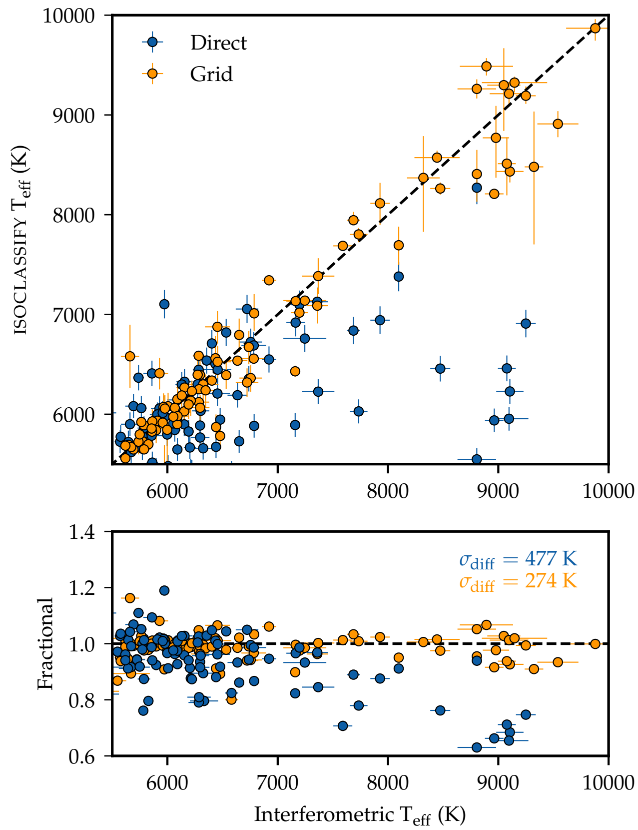

Figure 2. Comparison of effective temperatures derived with the ISOCLASSIFY direct (blue) and grid (orange) modes against interferometric temperatures from the CHARA sample, for stars hotter than 5500 K. The lower panel shows the fractional difference; the standard deviation of the ISOCLASSIFY–CHARA difference, $\sigma_{\rm diff}$, is indicated for each mode.

The empirical surface-brightness relations on which direct mode relies are also predominantly calibrated using FGK stars, with relatively few hot calibrators available. We therefore expect direct mode to systematically degrade in accuracy with increasing temperature, and we therefore used grid mode for our primary analysis.

3.1. *Validation against interferometry*

To verify that grid mode is suitable for our sample, we compared its output against interferometric effective temperatures. We assembled a comparison sample of 60 stars hotter than 5500 K that have published interferometric angular diameters from the CHARA array (T. S. Boyajian et al. 2012a,b, 2013; T. R. White et al. 2013, 2018), restricted to single, non-variable stars with *Gaia* DR3 counterparts. We used the published $F_{\rm bol}$ and $\theta_{\rm LD}$ values to calculate interferometric temperatures.

Figure 2 compares the ISOCLASSIFY direct- and grid-mode temperatures against the interferometric values. Direct mode shows a clear systematic deviation that grows with increasing temperature, with a standard deviation of 477 K about the one-to-one line and a tendency to under-predict $T_{\rm eff}$ for the hottest stars in the sample, with fractional discrepancies exceeding ∼40%. This is the expected consequence of the aforementioned diminishing color–temperature sensitivity, confirming that direct mode is unsuitable for this sample. Grid mode, by contrast, shows no significant temperature trend and a standard deviation of 274 K, comparable to typical A-type spectroscopic temperature uncertainties (S. J. Murphy et al. 2019). We therefore adopt grid-mode parameters throughout the remainder of this paper.

As a separate check of the grid-mode radius scale, we converted the ISOCLASSIFY-derived radius R and *Gaia* distance d into an implied angular diameter,

$$\theta_{\rm iso} = \frac{2R}{d}, \tag{1}$$

which we compared with the measured $\theta_{\rm LD}$. We found good agreement between $\theta_{\rm LD}$ and $\theta_{\rm iso}$ for the grid-mode sample, with a fractional scatter of $\sigma_\theta/\theta \approx 4.4\%$, consistent with the combined uncertainties. This angular-diameter comparison tests the inferred radius scale; because R was obtained from the grid-mode fit, it is distinct from the comparison with the independently published interferometric temperatures and is not itself a model-independent temperature validation.

3.2. *Grid-mode parameters for the full sample*

For each target in our A/F sample we ran ISOCLASSIFY in grid mode using the MIST isochrones (J. Choi et al. 2016; A. Dotter 2016). We used *Gaia* DR3 for parallax, G, $G_{\rm BP}$, and $G_{\rm RP}$ magnitudes, and the TIC $T_{\rm eff}$ as a loose prior with an inflated uncertainty of $\sigma_{T_{\rm eff}} = 300$ K to avoid over-weighting the photometric TIC temperatures. Extinctions are computed self-consistently within ISOCLASSIFY using the `combined19` dust map from the MWDUST package (J. Bovy et al. 2016a,b), which combines the D. J. Marshall et al. (2006), G. M. Green et al. (2015), and R. Drimmel et al. (2003) maps into a single all-sky three-dimensional reddening model. The output of each fit is a posterior distribution over $T_{\rm eff}$, log g, mass, radius, luminosity, and age, from which we adopted the median values as the point estimates and the 16th–84th percentile ranges as the uncertainties. We inflated the uncertainties of the temperature to be in agreement with the expected uncertainty from interferometry (∼ 300 K). These parameters form the basis of the analysis presented in the remainder of this paper.

4. IDENTIFYING δ SCUTI PULSATORS

Our goal is to identify δ Sct pulsators, in order to map the pulsator distribution across the instability strip and to compute the pulsator fraction. In contrast to the multi-class classification scheme of D. Hey & C. Aerts (2024), which simultaneously identified γ Dor, eclipsing,

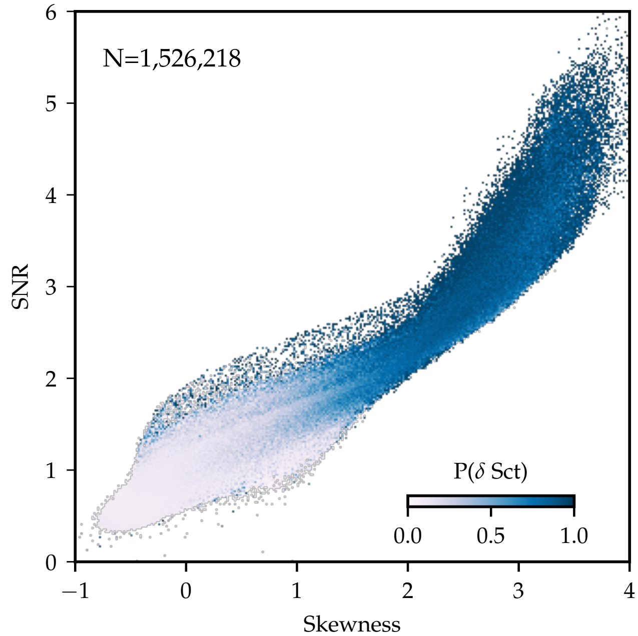

Figure 3. Distribution of targets in the spectral skew–SNR plane, colored by the score assigned by the PU classifier. Confirmed δ Sct pulsators occupy a well-defined locus at high skew and high SNR, separated from the bulk of unlabelled targets clustered at low values of both quantities.

and other OBAF variables using a random forest, here we attempt only to classify whether a target shows δ Sct-like pulsation or not.

A challenge with this classification is the absence of a curated negative class. Catalogues of manually vetted known δ Sct pulsators are extensive (A.-Y. Zhou 2023, 2025), but no comparably comprehensive list of confirmed non-pulsators within the instability strip exists, beyond extrapolation of S. J. Murphy et al. (2019). Any star not labelled as a δ Sct in the literature could equally be a genuine non-pulsator, an undetected low-amplitude pulsator, or simply a target that has never been inspected. Standard supervised classification assumes both positive and negative training labels are reliable, and treating unlabelled stars as negatives in this setting biases the resulting classifier toward under-predicting the positive class.

4.1. *Positive–Unlabelled classification*

We address this with a Positive–Unlabelled (PU) learning approach, recently introduced to asteroseismic classification by M. Kliapets et al. (2025). In the PU framework, a labelled set of confirmed positives is combined with a large unlabelled set containing an unknown mixture of true positives and true negatives. The classifier can then rank candidates without requiring every unlabelled target to be treated as a secure negative. This makes PU learning well suited to our problem, where the positive class (δ Sct variables) is well characterised but the unlabelled population mixes genuine non-pulsators with currently unclassified pulsators.

We classified these stars with the bagging PU algorithm of F. Mordelet & J.-P. Vert (2010), using a support vector machine (SVM; C. Cortes & V. Vapnik 1995) from `scikit-learn` (F. Pedregosa et al. 2011) as the base estimator.

4.2. *Features*

For each target we computed a small set of features summarising the Fourier spectrum and light-curve morphology, loosely based on those used by D. Hey & C. Aerts (2024). We used (i) the amplitude and frequency of the dominant Fourier peak above $5\,\mathrm{d}^{-1}$; (ii) the signal-to-noise ratio (SNR) of that peak relative to the 95th-percentile noise floor; (iii) the number of significant, independent peaks exceeding a false-alarm level of 1%; (iv) the skewness of the amplitude spectrum above $5\,\mathrm{d}^{-1}$; and (v) the skewness of the light curve. The first two capture the presence and location of coherent power in the δ Sct range, the third captures the multiperiodic character of the class, and the last two discriminate between the heavy-tailed amplitude distribution of a pulsator and the approximately symmetric distribution of a pure-noise spectrum.

Figure 3 illustrates the separability of the δ Sct class in the spectral-skew–SNR plane, which is a typical diagnostic (i.e., S. J. Murphy et al. 2019; S. Dholakia et al. 2024; A. K. Read et al. 2024). Confirmed pulsators occupy a well-defined region at high values of both quantities, while the bulk of unlabelled targets cluster at low skew and low SNR. The two populations overlap in a transition region that includes low-amplitude pulsators, where the PU classifier relies on the remaining features to make a decision.

4.3. *Training and validation*

The positive training set was taken from the manually-vetted *TESS* δ Sct catalogues of A.-Y. Zhou (2023, 2025), which together provide ∼100,000 confirmed pulsators covering the full sky within our adopted temperature range. To assess the purity of this catalogue, we randomly drew 1,000 targets, retrieved their TGLC light curves, and independently re-classified them by visual inspection of the light curve and amplitude spectrum. We found an agreement of 96%, with the small residual disagreement dominated by what appear to be borderline low-amplitude cases. We retained the full positive sample, noting that this residual contamination is small enough that its effect on the trained classifier is negligible compared to the contamination of the unlabelled set by undetected positives.

We held back 20% of the positive set as a validation sample, spanning the full range of apparent magnitude and effective temperature to ensure representative coverage of the feature space. We trained the classifier on the remaining 80%, together with the full unlabelled set. The final classifier achieved a recovery rate of 95% on the held-back positives with classification labels exceeding 0.9. However we point out that because the classifier is trained against unlabelled stars, $p_{\delta\,\mathrm{Sct}}$ is a ranking score. It is not a calibrated probability that a star is a δ Scuti pulsator, and we therefore choose the classification threshold empirically. Applying the classifier to the full sample of 1,526,218 stars and adopting a classifier threshold of $P(\delta\ \mathrm{Sct}) > 0.9$ yielded 156,706 δ Sct pulsators. Our threshold is based largely on the recovery of the held-back positives.

The PU classifier identifies any star whose periodogram is dominated by sharp, high-SNR Fourier peaks in the δ Sct frequency range, which can include sources of variability other than self-excited pressure modes. We therefore applied an additional cut. We removed known eclipsing binaries and ellipsoidal variables, whose orbital harmonics can populate the δ Sct frequency range and mimic pulsation features in the Fourier spectrum (L. W. IJspeert et al. 2024). To do this, we cross-matched our sample with the *TESS* Eclipsing Binary catalogue (A. Prša et al. 2022) and the *Gaia* DR3 eclipsing-binary catalogue (N. Mowlavi et al. 2023), removing $3,908$ targets in total. This cut necessarily removed genuine δ Sct variables in eclipsing systems; since the goal of this paper is a population-level analysis, and since the pulsation properties of such systems cannot be measured homogeneously alongside the single stars, we accepted this loss. The removed targets are flagged in the published catalogue.

5. THE H–R DIAGRAM AND PULSATOR FRACTION

Figure 4 shows the H–R diagram of the full sample, with classified δ Sct pulsators highlighted. The lower panel shows the δ Sct pulsator fraction computed in two-dimensional $(T_{\mathrm{eff}}, \log L)$ bins. The pulsators trace a clearly defined region that closely follows the classical instability strip, with a sharp red edge and a more diffuse blue edge. The evolutionary tracks shown there were computed as follows.

We used MESA r24.03.1 to calculate tracks with masses from 1.3 to $3.0\,\mathrm{M}_\odot$ in steps of $0.1\,\mathrm{M}_\odot$ at $Z = 0.0142$, corresponding to the bulk solar metallicity (M. Asplund et al. 2009), using the input physics and inlist template of A. Gatuam et al. (2026). We included rotation, from the ZAMS onwards, by first evolving the tracks without rotation from the pre-main sequence to 50 Myr. Their zero-age main sequence (ZAMS) ages were then located on that track with a variant of the stabilisation criterion of A. Gatuam et al. (2026). Specifically, for each of the effective temperature and the mean density we take the rolling standard deviation, over 100 consecutive models, of its smoothed second derivative with respect to age, and divide it by that quantity's threshold. The ZAMS is the first age at which the mean of these two ratios falls below one. This differs from the criterion as described by A. Gatuam et al. (2026) in dropping its $\Delta\nu$ term and in averaging the terms rather than requiring each to lie below its threshold. The model nearest the ZAMS is loaded into a new run, in which we switched on MESA's rotation and relaxed the star to uniform rotation at $\Omega = 0.4\,\Omega_{\mathrm{crit}}$. After relaxation, a uniform angular-momentum diffusion coefficient with MESA's default value, `uniform_am_nu_non_rot` $= 10^{20}\,\mathrm{cm}^2\,\mathrm{s}^{-1}$, was used to set a solid-body rotation profile, and $\Omega/\Omega_{\mathrm{crit}}$ is left to change as the star evolves. Neither rotational mixing of chemical elements nor mass loss was included. During the rotating evolution, MESA uses adaptive timesteps with a maximum of 2 Myr (`max_years_for_timestep` $= 2 \times 10^6$). We retained additional timestep controls using in $\log_{10} T_{\mathrm{eff}}$ and $\log_{10}(L/L_\odot)$, with `delta_lgTeff_limit` $= 0.0006$ and `delta_lgL_limit` $= 0.002$.

A MESA profile and its pulsation input file in the GSM format of GYRE were written at every fifth model and at the model on which the run stopped. For every profile, with no cut on evolutionary phase, we used STORM (V. Vanlaer (2026)) to compute mode frequencies for degrees $\ell \leq 3$, accounting for (uniform) rotation at the model's surface angular velocity Ω. We scanned 500 trial frequencies for each (ℓ, m), across a scan window of 0.25–$150\,\mathrm{d}^{-1}$. We ultimately used just the radial mode frequencies for this work.

5.1. *The observational instability strip*

To measure the edges of the observational instability strip, we require a smooth estimate of the pulsator fraction across the T_{eff}–$\log L$ plane. To construct this estimate we made use of a simple Gaussian convolution, which we now detail. We constructed bins of width (1.0, 2.0) in T_{eff}–$\log L$. Within each bin, (a, b), we counted the total number of stars n_{ab} and the number of δ Scuti pulsators k_{ab}, giving a fraction of $f_{ab} = k_{ab}/n_{ab}$. This estimator is binomial and its variance, $f(1-f)/n$, is dominated by the sparsely populated bins at the edges of the strip, producing jagged contours that preclude a direct edge fit. Rather than smoothing f_{ab} directly, which would equally weight small and large numbered bins, we convolved the count fields separately and took their ratio,

$$\hat{f} = \frac{G_{\boldsymbol{\sigma}} * k}{G_{\boldsymbol{\sigma}} * n}, \tag{2}$$

where $G_{\boldsymbol{\sigma}}$ is a Gaussian kernel and $*$ denotes convolution. This ensured that under-populated bins contribute negligibly to the contour. We adopted an anisotropic kernel, $\boldsymbol{\sigma} = (\sigma_{\log L}, \sigma_{T_{\mathrm{eff}}})$ with $\sigma_{\log L} > \sigma_{T_{\mathrm{eff}}}$. Because the strip edges are steep in temperature but not with increasing luminosity, smoothing more in the luminosity direction suppresses bin-to-bin noise while preserving the sharp temperature gradient that defines the edge, and adopt a $\sigma = (1.0, 2.0)$.

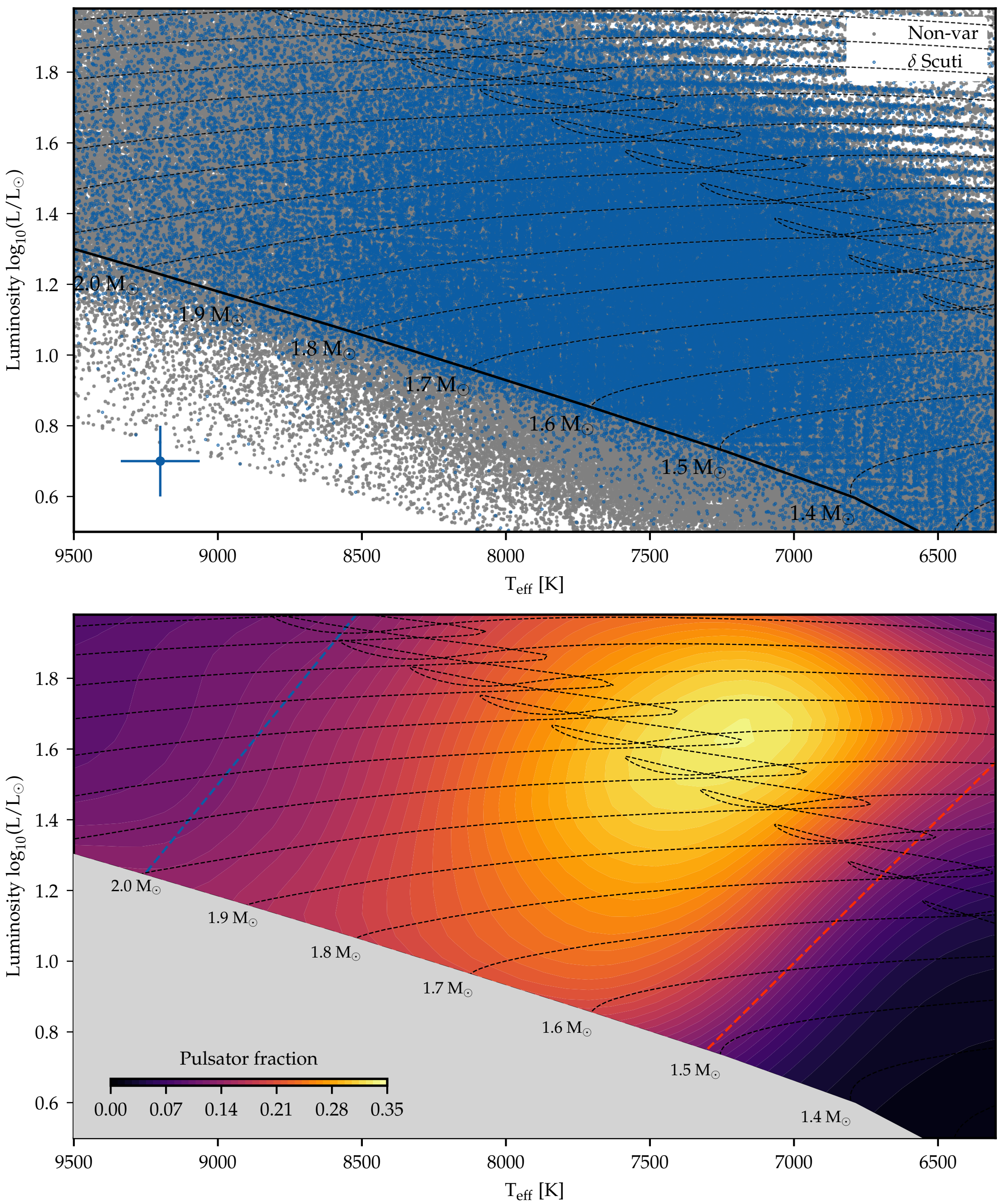

Figure 4. *Top:* H–R diagram of the full sample, including stars with classification probability < 0.9 (gray) and δ Sct candidates with a classifier score > 0.9 (blue). MIST evolutionary tracks are labelled by mass. *Bottom:* pulsator fraction in bins of $T_{\rm eff}$ and $\log(L/L_\odot)$, with bin boundaries restricted to contain at least 50 targets each. The peak pulsator fraction is $\sim 30\%$, reached near $T_{\rm eff} \approx 7150\,{\rm K}$.

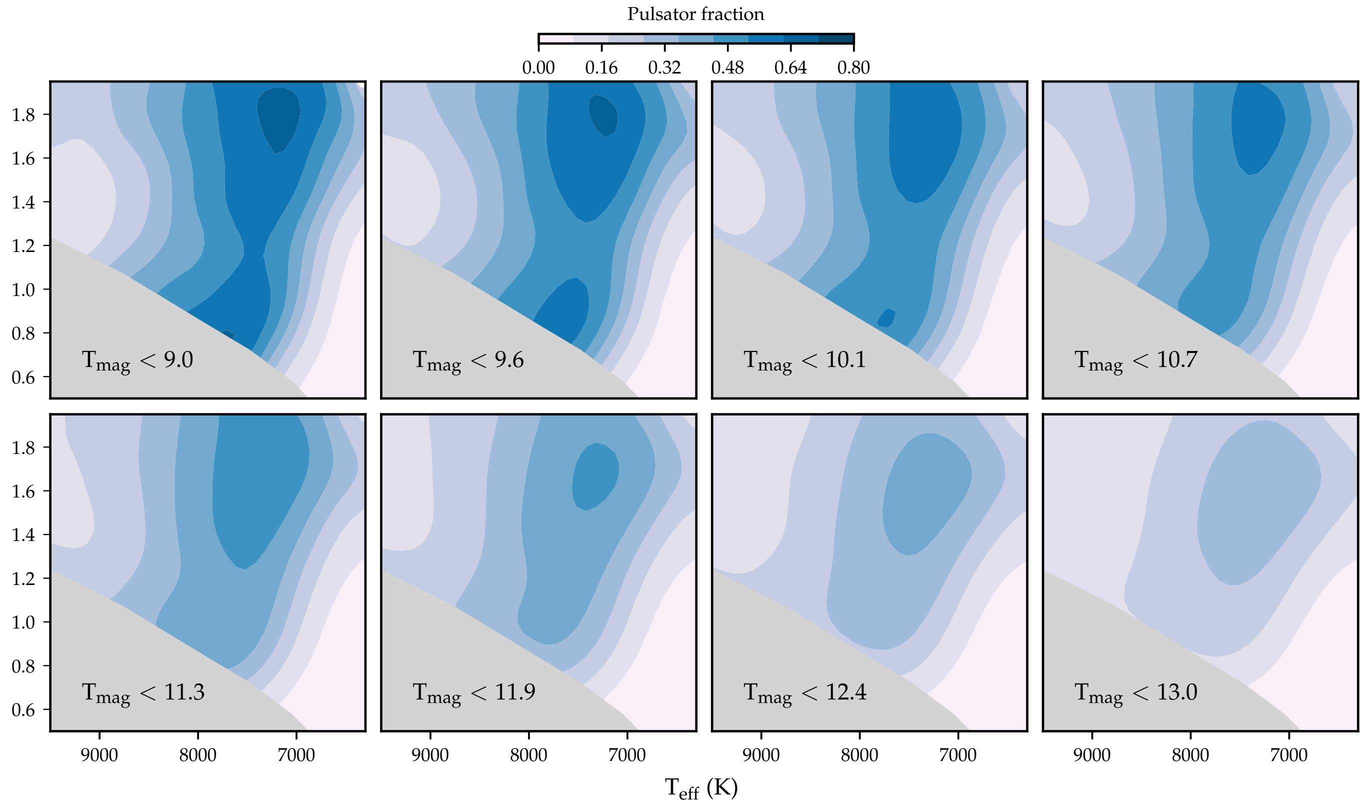

Figure 5. The pulsator fraction across the $T_{\rm eff}$–$\log(L/L_\odot)$ plane, computed for progressively fainter magnitude-limited subsamples. The peak fraction falls monotonically from $\sim 80\%$ for $T_{\rm mag} < 9.0$ to $\sim 20\%$ for $T_{\rm mag} < 13.0$.

The effective number of stars contributing to each smoothed pixel is

$$N_{\rm eff} = \frac{\left(\sum_{ab} w_{ab}\, n_{ab}\right)^2}{\sum_{ab} w_{ab}^2\, n_{ab}}. \tag{3}$$

Here, w_{ab} are the kernel weights, which we use both to propagate a per-pixel uncertainty, $\sigma_{\hat{f}} = [\hat{f}(1 - \hat{f})/N_{\rm eff}]^{1/2}$, and to mask regions with $N_{\rm eff} < N_{\rm min}$ where the fraction is too poorly constrained to trace an edge.

We defined the observational instability strip from this smoothed pulsator-fraction field, $\hat{f}$. Rather than adopting the fixed 20% contour used by S. J. Murphy et al. (2019), we chose the contour that encloses 80% of the detected pulsators, weighting each bin by its unsmoothed pulsator count. In each luminosity row, we linearly interpolated the red and blue crossings surrounding the local maximum in $\hat{f}$ and fitted linear relations to obtain

$$\log_{10}(L)_{\rm red} = -0.000669(\pm 0.0002) * {\rm T_{eff}} + 5.724(\pm 0.01) \tag{4}$$

$$\log_{10}(L)_{\rm blue} = -0.001030(\pm 0.0004) * {\rm T_{eff}} + 10.59(\pm 0.02). \tag{5}$$

The strip between these lines contains 80% of the detected pulsators for the entire sample.

We estimated the edge uncertainties with 1000 bootstrap realizations. In each step, we resampled the stars with replacement, perturbed their effective temperatures and luminosities according to their uncertainties, reconstructed the smoothed fraction map, and repeated the contour selection and edge fit. We adopted the median bootstrap edge as the fitted boundary and the 16th and 84th percentiles as its 68% confidence interval.

This full-sample calculation is a lower limit on the intrinsic pulsator fraction, because our sensitivity to low-amplitude pulsation degrades towards fainter magnitudes (see I. Berry et al. 2026). Figure 5 shows the pulsator fraction recomputed for a series of magnitude-limited subsamples. The peak fraction rises monotonically with brightness, from $\sim 20\%$ for the full $T_{\rm mag} < 13.5$ sample to $\sim 80\%$ for $T_{\rm mag} < 9.0$. The same trend was found by A. K. Read et al. (2024) in a color-restricted subsample of the same 10-min FFI data; they reported a pulsator fraction of $\sim$70% at $G < 8$ falling to $\sim$45% at fainter magnitudes. Subsequently, P. Mani et al. (2025) found a pulsator fraction of $\sim$70% for bright ($G < 7$) stars within one magnitude of the ZAMS. Our all-sky sample extends this behavior across the full strip and over a wider magnitude range.

The general morphology of the strip on the red end is preserved across all magnitude bins in Figure 5. That is, the peak remains at the same location in $(T_{\rm eff}, \log L)$ and the edges do not move appreciably, but its amplitude scales with detectability. This implies that the obser-

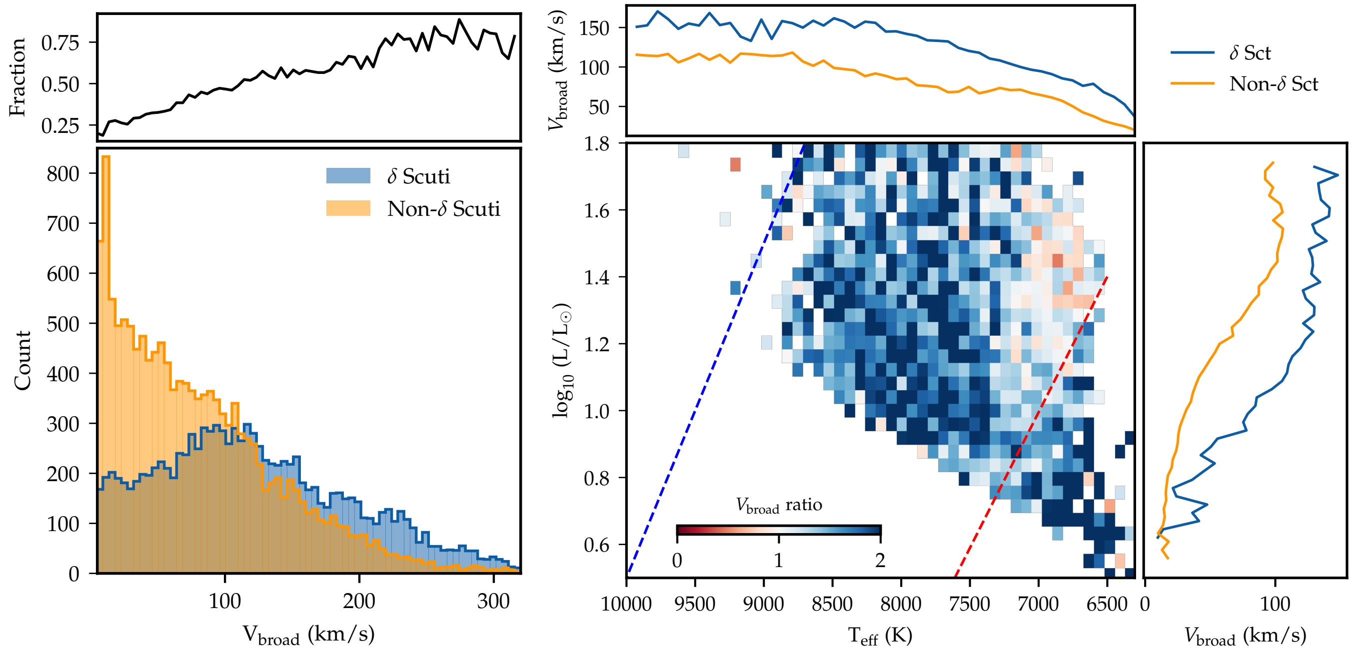

Figure 6. *Left:* distribution of `vbroad` for the two populations within the instability strip, with the pulsation fraction in the top panel. *Right:* the ratio of the median *Gaia* `vbroad` of classified δ Sct pulsators to that of non-pulsating stars, across the $T_{\rm eff}$–$\log(L/L_\odot)$ plane, for targets brighter than $T_{\rm mag} = 13$ and bins containing at least 5 δ Sct variables. Values above unity (blue) indicate that pulsators rotate faster than non-pulsators at the same position in the H–R diagram. The dashed lines mark the derived instability strip from Sec. 5.1. The marginal panels show the median `vbroad` of each population as a function of $T_{\rm eff}$ (top) and $\log L$ (right).

vational instability strip is considerably more populated than the full-sample fraction suggests, and a large part of the difference between our ∼30% and the ∼70% of L. A. Balona & W. A. Dziembowski (2011) and S. J. Murphy et al. (2019) is attributable to the shallower effective sensitivity of *TESS* FFI photometry relative to *Kepler* (cf. A. K. Read et al. 2024, who show that a single *TESS* sector reaches only ∼50 ppm at $G \approx 9$). Second, even in the brightest bin the peak fraction does not approach unity; ∼ 20% of stars at the centre of the strip remain undetected as pulsators. The strip is therefore not pure, but is more pure than the full-sample number would imply, and our result is consistent with the *Kepler*-based determinations.

5.2. *The influence of rotation*

Recent work has highlighted the role of rotation in shaping the δ Sct population (K. Gootkin et al. 2024; J. Wang et al. 2025; S. J. Murphy & A. Gautam 2026). Our larger sample, combined with the better frequency coverage of the 10-minute cadence, allows us to revisit this question with improved statistics.

Figure 6 shows the distribution of the *Gaia* `vbroad` line-broadening parameter for classified δ Sct pulsators and for non-pulsating stars within the instability strip, restricted to the subset of targets with `vbroad` measurements. The left panel shows that δ Sct variables are, on average, faster rotators than their non-pulsating counterparts. The median `vbroad` of δ Sct pulsators is $114\,{\rm km\,s^{-1}}$, compared with $68\,{\rm km\,s^{-1}}$ for the non-pulsators, and a two-sample Kolmogorov–Smirnov test rejects the null hypothesis that they are drawn from the same distribution. Critically, the right panel of Figure 6 shows that this offset is not an artefact of the two populations occupying different regions of the H–R diagram; the ratio of median `vbroad` exceeds unity across essentially the whole strip, so the effect holds at fixed $T_{\rm eff}$ and $\log L$.

The pulsator fraction increases monotonically with `vbroad` up to $\sim 200\,{\rm km\,s^{-1}}$ and plateaus at ∼ 75% for higher rotational velocities (Fig. 6), in agreement with K. Gootkin et al. (2024) and consistent with the expectation that rapid rotation inhibits the gravitational settling of helium out of the He II ionisation zone, sustaining the κ mechanism (S. Théado et al. 2011, 2005; S. Théado & S. Vauclair 2003a,b).

The existence of slowly rotating δ Sct pulsators, however, is not naturally accommodated by this picture. We find a pulsator fraction of ∼ 25% for stars with `vbroad` $< 50\,{\rm km\,s^{-1}}$, well within the regime where Am stars dominate. Some fraction of these will be rapid rotators seen close to pole-on, for which `vbroad` $\simeq v \sin i$ is small despite a large equatorial velocity. For an isotropic distribution of inclinations, however, only a small percentage of stars with high equatorial velocities would appear at low `vbroad` due to their inclination, which is in-sufficient to account for the observstions. The metallic-line character of these slowly rotating pulsators, and the corresponding helium abundance in their envelopes, will require spectroscopic follow-up before this population can be physically interpreted.

5.3. *Variability characteristics across the strip*

The 10-minute *TESS* cadence allows us to probe the δ Sct pulsation spectrum with a Nyquist frequency of $72\,\mathrm{d}^{-1}$, in contrast to the *Kepler* long-cadence ($24\,\mathrm{d}^{-1}$ Nyquist) and *TESS* 30-minute FFI ($24\,\mathrm{d}^{-1}$ Nyquist) datasets used in previous large-sample studies (S. J. Murphy et al. 2019; K. Gootkin et al. 2024). In those data, frequencies above the nominal Nyquist limit can appear as reflected aliases, and their observed amplitudes are reduced by smearing from the nonzero integration time (apodization; S. J. Murphy et al. 2013; H. Shibahashi & S. J. Murphy 2018; S. J. Murphy 2015). Although individual super-Nyquist modes can sometimes be recovered, attenuation complicates population-level selection. The 10-minute data move the Nyquist frequency to $72\,\mathrm{d}^{-1}$ and substantially reduce this problem, but do not eliminate it. Although modes above $72\,\mathrm{d}^{-1}$ remain aliased, we treat frequencies approaching the Nyquist limit as unaliased but amplitude-attenuated measurements Y. Mo et al. (2026).

Figure 7 shows the H–R diagram of pulsators color-coded by their dominant pulsation frequency. A clear gradient is visible across the instability strip, with cooler, less luminous pulsators near the red edge exhibiting dominant frequencies of ~ 10–$20\,\mathrm{d}^{-1}$, while hotter, more evolved pulsators near the blue edge cluster at ~ 50–$70\,\mathrm{d}^{-1}$. This trend is primarily the expected consequence of the scaling of acoustic mode frequencies with the square root of the mean stellar density (C. Aerts et al. 2010; M. Breger 2000): as stars evolve off the zero-age main sequence their radii increase and their mean density falls, lowering the frequency of any given radial order.

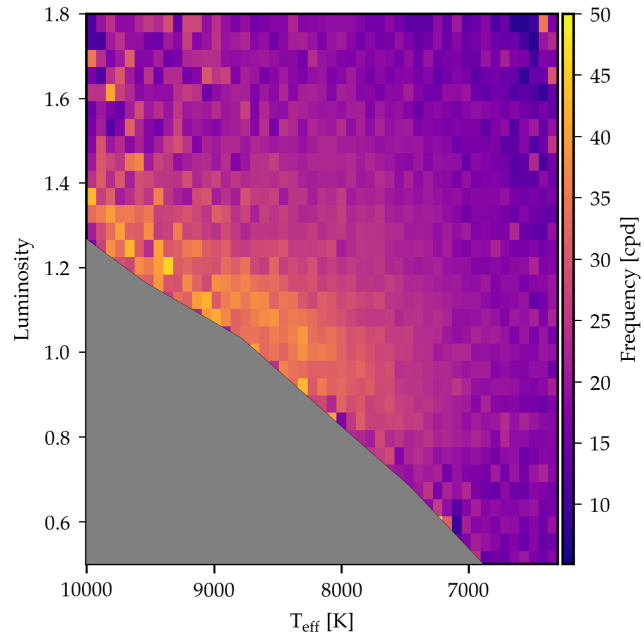

Figure 7. H–R diagram of classified δ Sct pulsators, color-coded by the frequency of the dominant Fourier peak. Cooler, less luminous pulsators near the red edge oscillate at lower frequencies, while hotter, more luminous pulsators near the blue edge exhibit higher dominant frequencies, consistent with the expected scaling with mean stellar density.

5.4. *Prewhitening the full sample*

To characterize the pulsation spectra beyond the dominant mode, we iteratively prewhitened each light curve of candidates with classifier score ≥ 0.9. At each iteration we identified the highest peak in the amplitude spectrum, optimized its frequency, amplitude, and phase by non-linear least squares against the residual light curve, subtracted the resulting sinusoid, and repeated until no peak exceeded a false-alarm probability of 1%. This process was identical to that of D. Hey & C. Aerts (2024). Peaks separated by less than $10^{-2}\,\mathrm{d}^{-1}$ from a stronger peak were treated as duplicates and removed. This process yielded 2,228,680 significant frequencies across our δ Sct sample.

The resulting joint distribution of frequency and amplitude is shown in Figure 8. The frequency distribution peaks at $f = 15.48\,\mathrm{d}^{-1}$ and is strongly right-skewed,

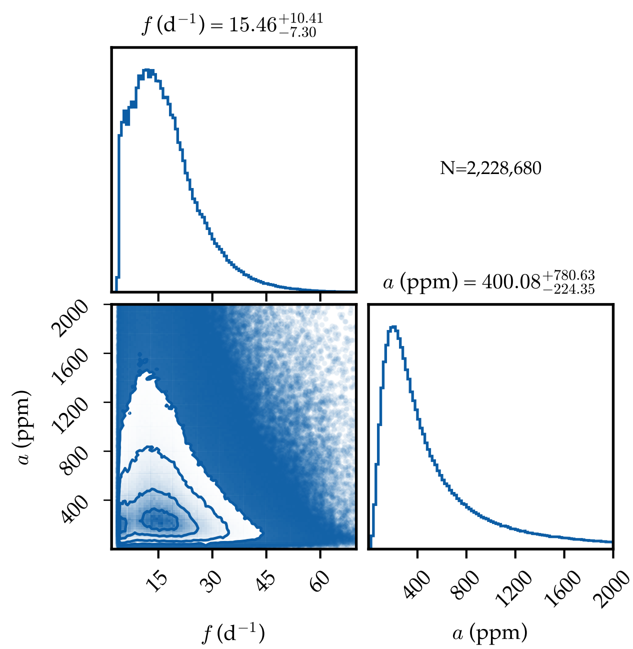

Figure 8. Joint distribution of extracted frequency f and amplitude a for all significant peaks prewhitened from the δ Sct sample with classifier score ≥ 0.9. The marginal distributions and their medians with 16th–84th percentile ranges are shown in the upper and right panels.

with a tail extending to the Nyquist limit; the amplitude distribution is approximately log-normal, centred on a median amplitude of ~ 400 ppm. There is a weak correlation between frequency and amplitude across the population, with increasing frequencies corresponding to lower amplitudes, indicating that the amplitude distribution of excited modes is weakly dependent of where in the δ Sct frequency range they lie (e.g., L. A. Balona 2018; D. M. Bowman & D. W. Kurtz 2018; P. Mani et al. 2025).

6. THE PERIOD–LUMINOSITY AND PERIOD–DENSITY RELATIONS

The δ Sct variables, like other types of p-mode pulsators, exhibit a period–luminosity (PL) relation (D. H. McNamara 2011). This arises from the more fundamental relation between period and density (e.g., M. Catelan & H. A. Smith 2015), as characterized by the pulsation constant

$$Q \;=\; P\left(\frac{\bar{\rho}}{\bar{\rho}_\odot}\right)^{1/2}. \tag{6}$$

Here, P is the pulsation period and $\bar{\rho}$ is the mean stellar density (M. Breger 2000). For a given mode, Q is approximately constant across the δ Sct class. The period of this mode is set by the star's mean density, which explains the period–density relation. On the main sequence, density scales approximately with luminosity, which explains the existence of the PL relation. Here we present both, but emphasise the period–density relation (as in P. Mani et al. 2025), which links directly to Equation 6.

For all of the fits we made the following cuts on our data. We selected stars with classifier probability $p_{\rm class} \geq 0.90$, dominant-peak SNR ≥ 10, and catalogue spectral-skewness statistic `logskewa` ≥ 1.5. We additionally required a positive parallax with $\sigma_\varpi/\varpi < 0.05$, RUWE < 1.4, $-1.8 \leq \log_{10}(P_{\rm dom}/{\rm d}) \leq -0.8$, $\sigma_{\log L} \leq 0.15$ dex, and $\sigma_{M_G} \leq 0.30$ mag. For the period–luminosity fit, we also required that the adopted extinction satisfy $0 \leq A_V \leq 5$ mag and the inferred intrinsic color $-0.2 \leq (G_{\rm BP}-G_{\rm RP})_0 \leq 1.5$. These cuts left 93,971 stars.

6.1. *Period–density relation*

We begin with the period–density fit, shown in Fig. 9. Assuming constant-Q sequences, we define

$$x \equiv \log_{10}\frac{P}{d}, \tag{7}$$

$$y \equiv \log_{10}\frac{\rho}{\rho_\odot}, \tag{8}$$

such that

$$y = -2x + 2\log_{10} Q. \tag{9}$$

Recasting the period–density relation to this form is useful for recovering the pulsation constants directly (as in S. J. Murphy & A. Gautam 2026). Rather than fitting arbitrary straight lines in the (x, y) plane, we instead impose a fixed slope from Eq. 9 and project each star into the one-dimensional coordinate

$$q \equiv x + \frac{1}{2}y = \log_{10}\frac{Q}{d}. \tag{10}$$

Note that this is equivalent, within a multiplicative constant, to measuring the perpendicular distance to a line with slope -2 (see E. Ziaali et al. 2019; N. Barac et al. 2022; A. K. Read et al. 2024; P. Mani et al. 2025).

Every parallel constant-Q ridge becomes a peak in the q distribution, and its mean μ maps back to a line with intercept 2μ in Eq. 9, and as seen in Fig. 9. This formulation fits the relevant quantity Q directly, and reduces the problem to fitting an arbitrary sum of mixed Gaussian distributions, allowing us to easily incorporate background distributions.

We modeled the distribution of q as a sum of K Gaussian ridge components plus a broad Gaussian background:

$$p(q_i) = \sum_{k=1}^{K} \omega_k \mathcal{N}(q_i|\mu_k, s_{i,k}) + \omega_{\rm bg}\mathcal{N}(q_i|\mu_{\rm bg}, s_{i,{\rm bg}}) \tag{11}$$

where $s_{i,k}$ is the standard deviation characterizing the width of the kth ridge. The broad component absorbs non-radial modes, higher radial orders, and contaminants. We maximized the likelihood of this model and compared models with $K = 1, 2, 3$ Gaussian mixtures using the Bayesian Information Criterion (BIC; G. Schwarz 1978). A single ridge is strongly disfavoured, as is plainly obvious from Fig. 9 ($\Delta BIC = 2401$), while the two- and three-ridge models have similar BIC values (-49524 and -49589, respectively). For simplicity, we adopted the two-ridge model, while noting that it is possibly a combination of several higher-order overtones (i.e., 3O + 4O) and unresolved binaries, which we discuss further below. We label the high-Q sequence as the fundamental mode (F) and the lower-Q sequence as a secondary ridge (S).

For the two-ridge mixture, we obtained $Q_F = 0.029216 \pm 0.0001$ and $Q_S = 0.016892 \pm 0.0001$, giving corresponding period–density relations of

$$\begin{aligned}\log_{10}(\rho/\rho_\odot)_{\rm F} &= -2\log_{10}\left(\frac{P}{d}\right) - 3.0616,\\ \log_{10}(\rho/\rho_\odot)_{\rm S} &= -2\log_{10}\left(\frac{P}{d}\right) - 3.6048.\end{aligned} \tag{12}$$

The separation between the ridges is 0.2716 dex in $\log P$ at fixed density, or 0.5432 dex in $\log \rho$ at fixed period, and their ratio is $Q_{\rm S}/Q_{\rm F} = 0.578$. The fundamental ridge lies close to, but below the commonly adopted fundamental value of $Q = 0.033$ d. This difference could potentially be caused by population variation in Q or a systematic offset in the density scale, which we now discuss.

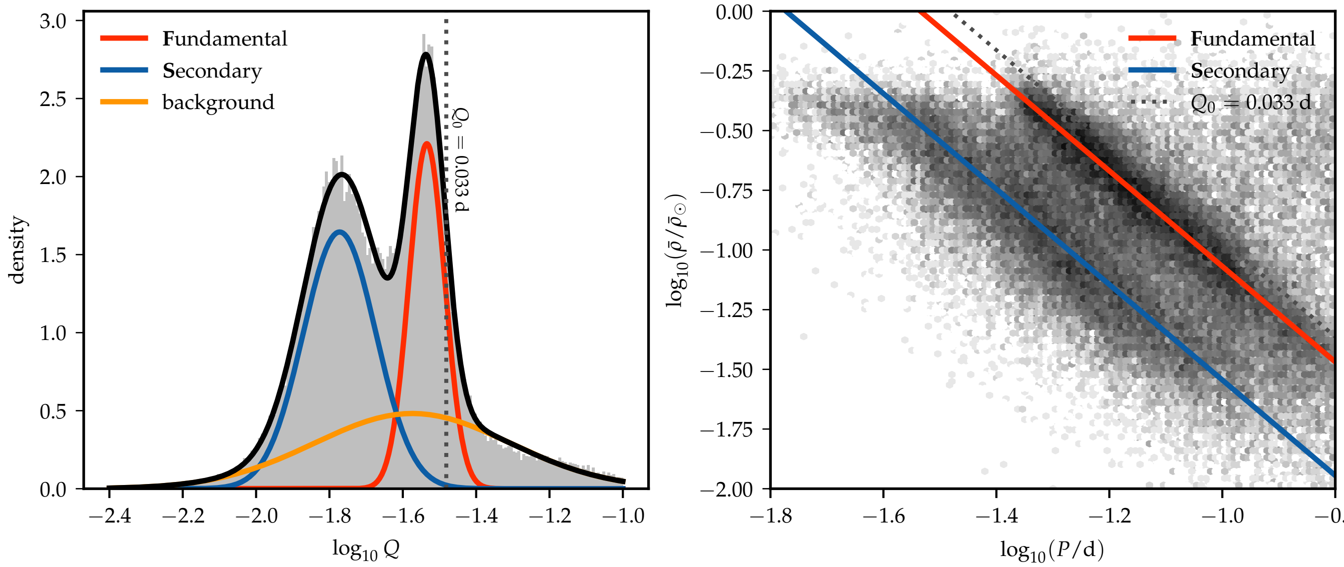

Figure 9. *Left*: The representative pulsation constant Q of the sample following Eq. 10, fit with three Gaussian distributions corresponding to the fundamental (red), secondary (blue), and background ridges. The dashed black line marks the canonical fundamental mode pulsation constant (M. Breger 2000). *Right*: The period–density relation with the straight lines obtained from the Gaussian means to the pulsation constant.

The second sequence has been previously identified in the δ Sct period–luminosity diagram by E. Ziaali et al. (2019) and N. Barac et al. (2022). Taking the high-Q sequence to be the radial fundamental, its value can be compared directly with the $Q_{\mathrm{F}} = 0.0315$ suggested by N. Barac et al. (2022) from *Kepler* data. Our value is slightly lower but both are within the uncertainty. From the tracks used in Sec. 4, we calculate a mass-dependent Q_F between 0.0311 and 0.0329, quite far below the canonical value and close to that of N. Barac et al. (2022). Our value lies slightly below this range, and we note that the PL relation investigated in N. Barac et al. (2022) was performed with *Kepler* data of a much higher photometric quality.

The ratio between the two sequences we measure is $Q_{\mathrm{S}}/Q_{\mathrm{F}} = 0.578 \pm 0.001$. The ratio is a useful value to consider here because it is invariant under any rescaling of the density zero point. That is, a systematic error in $\bar{\rho}$ (or period, for that matter) displaces both sequences equally in $\log_{10} Q$ and leaves their ratio unchanged. Our ratio is slightly larger than the value reported by E. Ziaali et al. (2019) and N. Barac et al. (2022), who measured the second ridge to be a factor of two shorter in period. They suggested it might arise from a 2 : 1 resonance between the fundamental mode and either the third or fourth overtone. Our ratio is largely consistent with this result. The theoretical values for $Q_2/Q_0 = 0.621$ and $Q_3/Q_0 = 0.515$ straddle our measured ratio (J. P. Cox et al. 1972). Likewise, S. J. Murphy & A. Gautam (2026) recently argued that the second ridge is satisfactorily reproduced with a mixture model consisting of the same 2:1 resonance, and a term representing a combination frequency of the fundamental and first overtone modes.

6.2. *Period–luminosity relation*

The period–luminosity relation for the dominant mode in our sample is shown in Fig. 10, using the luminosities returned by `isoclassify`. We fitted the ridges in both the `isoclassify` reported luminosity, and Gaia absolute magnitude M_G. We calculated the extinction-corrected absolute magnitude as

$$M_{G,0} = G - A_G + 5\log_{10}\left(\frac{\varpi}{\mathrm{mas}}\right) - 10, \tag{13}$$

where ϖ is the *Gaia*-DR3 parallax and A_G is obtained from the line-of-sight V-band extinction A_V, as returned by the `isoclassify` posterior. Because the *Gaia* passband is broad, the ratio A_G/A_V is not constant but depends on the intrinsic color (and reddening) of the star. We thus adopted the polynomial coefficients of K. L. Luhman & T. L. Esplin (2020) who fitted $A_{G,\mathrm{BP},\mathrm{RP}}/A_V$ as functions of the de-reddened Gaia color. We detail the process of obtaining A_G in Appendix A.

Given our values of temperature, luminosity, and $\mathrm{M}_{G,0}$, we fitted both sequences simultaneously with a linear relation in log space, using a common slope while each ridge has its own zero point. Each measurement uncertainty was added in quadrature to the corresponding intrinsic scatter. Quoted statistical intervals are the 16th–84th percentiles of 100 bootstrap resamples.

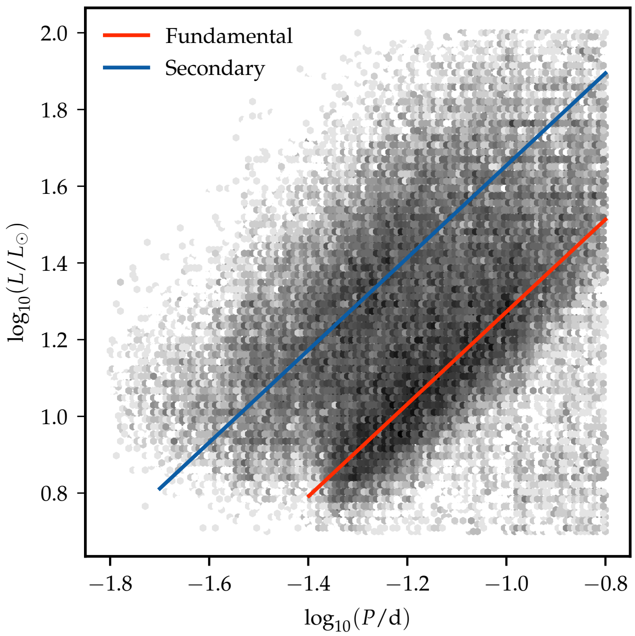

Figure 10. The period luminosity relation and corresponding fits for the fundamental (red) and secondary (blue) ridges.

The fitted G-band relations are

$$M^{\rm F}_{G,0} = \left(-3.041^{+0.012}_{-0.015}\right)\log_{10}\left(\frac{P}{\rm d}\right) - 1.542^{+0.014}_{-0.017},$$
$$M^{\rm S}_{G,0} = \left(-3.041^{+0.012}_{-0.015}\right)\log_{10}\left(\frac{P}{\rm d}\right) - 2.486^{+0.017}_{-0.019}, \quad (14)$$

with intrinsic scatters of 0.252 and 0.320 mag, respectively. The shared slope is broadly consistent with the approximately −3 slopes obtained in previous radial-mode calibrations, although direct comparisons certainly depend on the passband and sample definition (D. H. McNamara 2011; E. Ziaali et al. 2019; T. Jayasinghe et al. 2018; N. Barac et al. 2022; F. Guo et al. 2025; Q. Jia et al. 2025; S. J. Murphy & A. Gautam 2026).

Fitting luminosity in the same way gives

$$\log_{10}\left(\frac{L_{\rm F}}{L_\odot}\right) = \left(1.204^{+0.007}_{-0.004}\right)\log_{10}\left(\frac{P}{\rm d}\right) + 2.476^{+0.008}_{-0.004},$$
$$\log_{10}\left(\frac{L_{\rm S}}{L_\odot}\right) = \left(1.204^{+0.007}_{-0.004}\right)\log_{10}\left(\frac{P}{\rm d}\right) + 2.858^{+0.009}_{-0.006}, \quad (15)$$

with intrinsic scatters of 0.104 and 0.127 dex. We show this fit in Fig. 10. Equivalently, adopting $M_{\rm bol,\odot} = 4.74$, the bolometric relations have a shared slope of −3.009 and zero points of −1.450 and −2.404 mag. The fitted zero-point separation corresponds to a horizontal displacement $\Delta\log P = -0.310$ dex in $M_{G,0}$, or $P_{\rm S}/P_{\rm F} = 0.489^{+0.003}_{-0.001}$; the luminosity fit independently gives $0.482^{+0.002}_{-0.001}$. Again, these ratios are much closer to a third- or fourth–overtone than a first-overtone sequence.

6.3. *Rotational broadening and proximity to the radial-mode ridges*

Color-coding the period–density relation by the *Gaia* DR3 line-broadening parameter $v_{\rm broad}$ (Figure 11, left) reveals that stars lying closest to the fundamental ridge has, on average, the lowest $v_{\rm broad}$, and that the distance of a star from the nearest ridge tends to increases with its rotational broadening. We interpret this correlation as the combined signature of two rotation-related effects that act, respectively, on the mode that is measured, on the density that is inferred, and on the pulsation frequency itself.

Firstly, the main ridge is populated by stars in which the fundamental radial mode is the dominant mode. The high-amplitude δ Scuti stars, which obey the period–density relation most tightly, are predominantly slow rotators ($v\sin i \lesssim 30$ km s^{-1}; M. Breger 2000), whereas rapid rotators are overwhelmingly low-amplitude, multiperiodic pulsators dominated by non-radial modes (F. Royer et al. 2007). For the latter, the highest-amplitude peak often does not correspond to the fundamental radial mode, so the period shown in the diagram does not lie on that ridge. A substantial part of the trend with $v_{\rm broad}$ is therefore a mode-selection effect rather than a dynamical displacement.

Relatedly, the mean density is inferred from the luminosity and effective temperature under the assumption of a spherical, non-rotating star. Rapid rotation breaks this assumption, such that centrifugal flattening reduces the mean stellar density (S. J. Murphy et al. 2026) and gravity darkening renders the apparent L and $T_{\rm eff}$ dependent on the unknown inclination (H. von Zeipel 1924; F. E. Lara & M. Rieutord 2011), with a star viewed pole-on appearing hotter and more luminous than the same star seen equator-on. Because the inclination is effectively random across the sample, rotation introduces an inclination-dependent scatter that can reach ∼ 0.1 dex in $\log\bar{\rho}$ at moderate rotation rates, which is comparable to the ∼ 0.12 dex separation between the fundamental and first-overtone ridges. This effect scatters rapid rotators to either side of a ridge rather than displacing them coherently (A. García Hernández et al. 2024).

Finally, rotation perturbs the pulsation frequencies directly. Centrifugal distortion inflates the star and lowers its true mean density, lengthening the radial periods, while the Coriolis force shifts and splits the non-radial modes (C. Aerts et al. 2010; J. C. Suárez et al. 2006; Z. Guo et al. 2024). These effects are second order in the rotation rate, $\propto (\Omega/\Omega_{\rm crit})^2$, and displace a star from the non-rotating constant-Q relation by up to a few hundredths of a dex at the rotation rates typical of the sample.

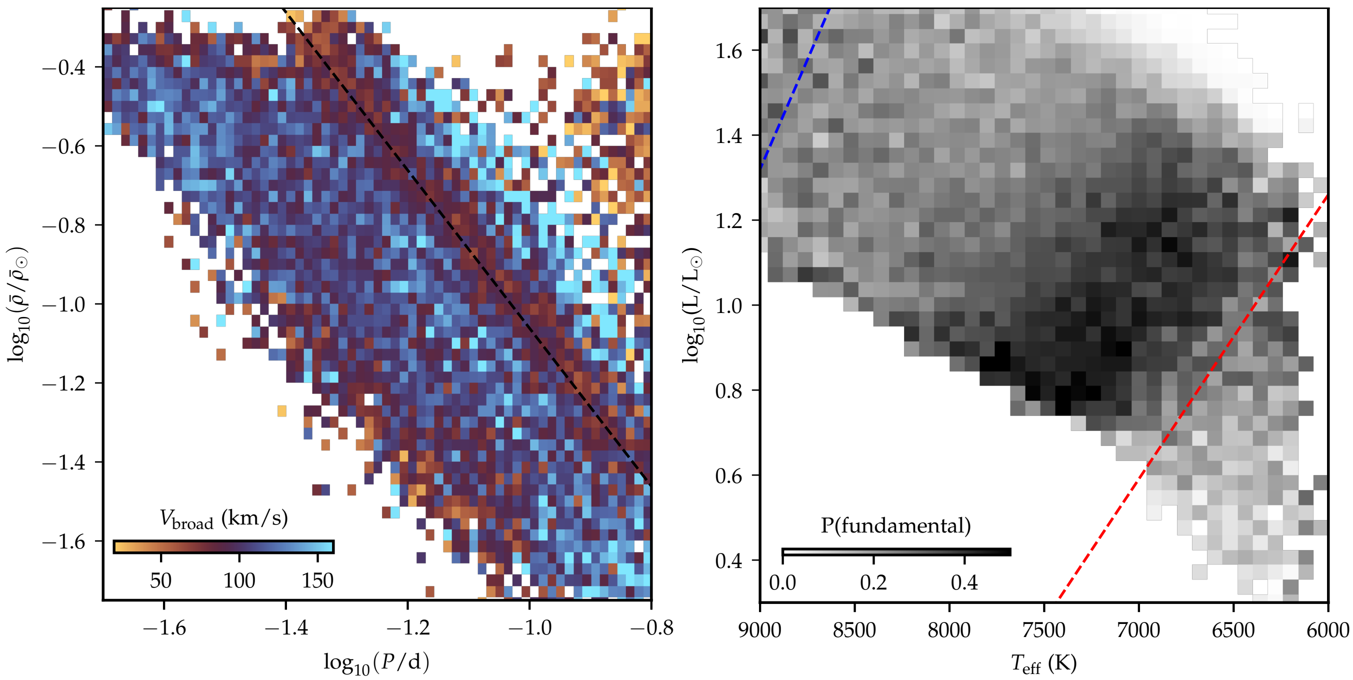

Figure 11. *Left:* The period-density relation colored by median `vbroad`, with the fundamental ridge marked by a dashed black line. *Right:* The δ Sct sample in the H–R diagram, colored by probability of belonging to the fundamental radial ridge in the period–density relation. The dashed lines are the instability strip from Sec. 5.1.

These two effects combine to produce the trends with $v_{\rm broad}$ seen in the left panel of Figure 11.

6.4. *Stars near the fundamental-mode ridge*

We now use the probability of belonging to the fundamental ridge as an empirical diagnostic of where such stars lie within the instability strip. In Sec. 6.1, we fitted a sum of Gaussians to determine the probability of each star belonging to either the fundamental, secondary, or background distributions. The right panel of Figure 11 shows the H–R diagram of the δ Sct sample binned according to their probability of belonging to the fundamental ridge. The stars more likely to belong to the ridge are not distributed uniformly across the strip; they are concentrated towards the cool, low-luminosity corner near the red edge. The remaining stars appear to populate the hotter and more luminous region towards the blue edge. This pattern is consistent with the rotation picture developed above, because the cool, low-luminosity part of the strip contains many of the slowest rotators and HADS stars. It also implies that a PL relation calibrated from ridge-proximate stars samples a restricted region of the instability strip, a caveat for distance-scale applications. We stress that ridge proximity alone does not uniquely identify the radial fundamental: non-radial modes and rotationally shifted modes can overlap the ridge, while independently identified radial-fundamental pulsators may lie elsewhere in the diagram.

7. δ Sct PULSATORS IN OPEN CLUSTERS

In Sec. 5.3 we examined how the mean frequency of δ Sct stars decreases as the star evolves. Such a relation naturally invites us now to investigate how the mean pulsation frequencies of δ Sct stars change within clusters. Open clusters offer a powerful laboratory for the study of δ Sct pulsations. Cluster members share a common age, distance, and initial chemical composition to within small dispersions, allowing the intrinsic variations in pulsation properties at fixed stellar parameters to be isolated from the population-level scatter that dominates the field-star sample analysed in Section 5. Several recent studies have exploited *Kepler*, K2 and *TESS* data to characterize the δ Sct populations of individual clusters (e.g., E. Rodríguez et al. 2020; S. J. Murphy et al. 2022; T. R. Bedding et al. 2023; D. P. Ortega et al. 2023; D. B. Palakkatharappil & O. L. Creevey 2023; G. Li et al. 2024; S. J. Murphy et al. 2024b; I. Berry et al. 2025; A. Dileep et al. 2025; D. M. Mwanzia et al. 2025; M. Qin et al. 2026; M. Soares-Furtado et al. 2026; A.-Y. Zhou 2025, I. Berry et al., submitted), but a homogeneous analysis across the full set of clusters observable by *TESS* has so far not been completed. With *Gaia* DR3 we now have cluster membership catalogues based on *Gaia* astrometry which provide a homogeneous, all-sky foundation for population-level cluster asteroseismology.

7.1. *Cluster cross-matching*

We cross-matched our full target sample against the *Gaia* DR3 open cluster catalogue of E. L. Hunt & S.

Name	N	$N_{\delta\,\rm Sct}$	Age (Myr)
NGC 3532	3414	75	238^{+218}_{-93}
NGC 2516	3784	64	125^{+127}_{-52}
NGC 5822	804	35	1040^{+643}_{-330}
NGC 6475	1427	34	171^{+163}_{-59}
NGC 2423	571	31	1182^{+771}_{-348}
NGC 2360	1188	30	1451^{+703}_{-492}
NGC 2477	3543	29	701^{+358}_{-212}
NGC 1662	384	21	345^{+243}_{-128}
NGC 2287	948	21	154^{+130}_{-58}
NGC 6405	974	19	52^{+39}_{-22}
Trumpler 10	1425	18	37^{+25}_{-18}
NGC 2527	389	17	820^{+565}_{-292}
NGC 2422	1129	17	109^{+87}_{-46}
Alessi 6	203	16	366^{+210}_{-127}
OC 0588	409	14	232^{+164}_{-95}
NGC 2447	1043	14	740^{+449}_{-289}
ASCC 90	184	14	409^{+240}_{-148}
HSC 1553	330	13	38^{+25}_{-21}
BH 99	643	13	45^{+43}_{-19}

Table 1. The 20 most populous clusters in our sample, where the classifier probability exceeds 90%. Here, N is the number of stars in the cluster and $N_{\delta\ \rm Sct}$ is the number of classified δ Sct variables. Ages are from E. L. Hunt & S. Reffert (2023). We make available the full table and membership list in electronic format online.

Reffert (2023), which provides homogeneous membership probabilities, ages, distances, and metallicities for 7167 clusters identified from *Gaia* astrometry. We retained stars with membership probability $p_{\rm mem} > 0.7$ to minimize contamination from field stars, and we further restricted the cluster sample to those with at least five δ Sct candidates within our analysis sample. This yielded 82 clusters containing 1,079 δ Sct pulsators in total, spanning ages from $\log(t/{\rm yr}) = 7.0$ to 9.5. The twenty most populous clusters are listed in Table 1, and we make the full catalog available in machine-readable format.

7.2. *Mean pulsation frequency as an age tracer*

For each cluster we computed the mean pulsation frequency $\langle\nu_{\rm max}\rangle$ of its δ Sct members. For an individual star, we defined this to be the amplitude-weighted mean of its prewhitened frequencies (S. Barceló Forteza et al. 2020; S. J. Murphy et al. 2024a), and the cluster value is the unweighted mean over its members. Figure 12 shows cluster age against $\langle\nu_{\rm max}\rangle$. There is an obvious correlation where clusters younger than ~ 100 Myr have mean pulsation frequencies of ~ 30–$50\,{\rm d}^{-1}$, while clusters older than ~ 1 Gyr cluster at ~ 10–$20\,{\rm d}^{-1}$. We regressed $\log t$ on $\log \nu_{\rm max}$, which is the direction in which the relation could be used (see below), and obtained

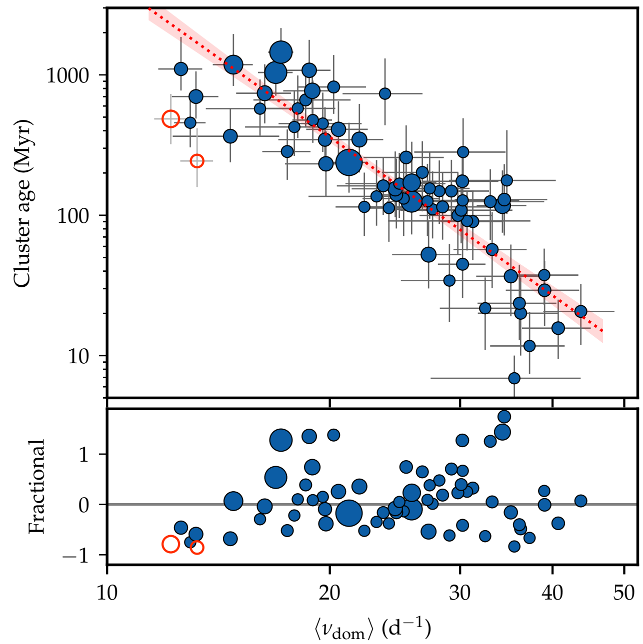

Figure 12. Cluster age as a function of mean pulsation frequency. Each point represents a single cluster, with the marker size scaled by the number of δ Sct members and the error bars showing the standard error on the mean frequency and the catalogue age uncertainty. The dotted line shows the best-fit linear relation (excluding the two clusters shown as red symbols), and the lower panel shows the fractional residual.

$$\log\left(\frac{t}{\rm yr}\right) = -3.75(\pm0.36)\,\log\left(\frac{\langle\nu_{\rm max}\rangle}{{\rm d}^{-1}}\right) + 13.43(\pm0.51), \quad (16)$$

with an intrinsic scatter of $\sigma_{\log t} \approx 0.09$ dex. The fit carries the uncertainty on both coordinates together with an intrinsic-scatter term. Two clusters (red circles in Figure 12), Ruprecht 98 and NGC 2099, were rejected by a 3σ clipping, leaving 67 clusters in the fit. The physical origin of this correlation is well understood from the fact that mean stellar density decreases with age, such that the average frequency also decreases.

Much of the substantial scatter about this relation presumably arises from the star-to-star variation of which modes are excited within each cluster, as seen with *TESS* in the Pleiades (T. R. Bedding et al. 2023), NGC 2516 (G. Li et al. 2024), NGC 3532 (I. Berry et al. 2025), and the Cep-Her complex (S. J. Murphy et al. 2024a). Nevertheless, the empirical relation in Eq. 16 offers a practical age indicator for young to intermediate-age clusters that complements traditional isochrone fitting. Isochrone-based ages rely on accurate photometric calibration, well-constrained extinction, and reliable main-sequence-turnoff identification, all of which can be problematic for sparsely populated or heavily reddened clusters. The δ Sct mean-frequency age, by contrast, requires only that several δ Sct pulsators be identified within the cluster and that their dominant frequencies be measured, both of which are straightforward with *TESS* 10-min FFI data. For an arbitrary cluster, the relation returns an age to $\sigma_{\log t} \approx 0.2\,\mathrm{dex}$, which is a factor of 1.5, so that a 500 Myr cluster is placed between 330 and 760 Myr. This is comparable to the median uncertainty of 0.23 dex on the catalogue ages themselves, and to the precision achieved by careful isochrone fitting for similar clusters (D. Bossini et al. 2019; T. Cantat-Gaudin et al. 2020).

This relation is defined by the mean dominant frequency, $\langle\nu_{\max}\rangle$, and is therefore sensitive to small-number statistics in clusters with few δ Sct members. We have restricted our analysis to clusters with at least five identified pulsators to mitigate this but the youngest and oldest clusters in our sample, where δ Sct stars are rare, carry correspondingly larger uncertainties. Secondly, metallicity is expected to influence both the location of the instability strip and the pulsation frequencies of stars within it (S. J. Murphy et al. 2019; S. J. Murphy & A. Gautam 2026). Thirdly, rapidly rotating δ Sct stars exhibit modified pulsation frequencies due to rotational distortion (Section 6.3); the impact of rotation on cluster-mean frequencies will require further investigation with a larger sample, which we identify as an avenue for future work.

8. CONCLUSIONS

We have presented a large, uniform asteroseismic survey of A- and F-type stars, comprising 1,526,218 stars in and around the classical δ Sct instability strip observed by *TESS* at 10-minute full-frame image cadence over most of the sky. The $72\,\mathrm{d}^{-1}$ Nyquist frequency greatly reduces the aliasing that affects 30-minute data, while *Gaia* DR3 parallaxes and isoclassify fits provide homogeneous stellar parameters across the sample. Comparisons with interferometric temperatures and angular diameters support the adopted temperature and radius scales, with the residual scatter described in Section 3.1. Our results are as follows.

- The δ Sct instability strip is not pure at the detection threshold of this survey, but the apparent impurity is strongly magnitude-dependent. The peak pulsator fraction is $\sim 30\%$ for the full sample and rises to $\sim 80\%$ for $T_{\mathrm{mag}} < 9$, where our amplitude sensitivity is greatest. Detection sensitivity therefore accounts for much of the difference between our full-sample fraction and the $\sim 60\%$ inferred from *Kepler* (L. A. Balona & W. A. Dziembowski 2011; S. J. Murphy et al. 2019). Even at the bright end, the detected fraction does not reach unity, confirming that a genuine population of non-δ Sct stars pervades the strip.
- δ Sct pulsators are systematically faster rotators than non-pulsating stars at the same position in the H–R diagram, with the pulsator fraction increasing monotonically with the *Gaia* `vbroad` parameter. This confirms the findings of S. J. Murphy et al. (2024b); K. Gootkin et al. (2024); J. Wang et al. (2025) with a larger sample and unambiguous frequency coverage. A population of δ Sct pulsators with `vbroad` $< 50\,\mathrm{km\,s^{-1}}$ persists, larger than can be explained by inclination effects alone, and requires spectroscopic follow-up.
- We refine the δ Sct period–density and period–luminosity relations, finding results largely consistent with previous determinations (D. H. McNamara 2011; E. Ziaali et al. 2019; N. Barac et al. 2021). Recast as a period–density relation, two approximately parallel ridges are resolved with a ratio of pulsation constants of 0.578, corresponding to a likely combination of excited overtone modes.
- Stars lying closest to the radial-mode ridge have systematically lower `vbroad`, and the distance from the ridge increases with rotational broadening. We attribute this to a combination of mode selection (rapid rotators are dominated by non-radial modes), inclination-dependent bias in the inferred mean density from gravity darkening, and direct second-order rotational perturbation of the frequencies. These fundamental-mode pulsators occupy a cooler, less luminous subregion of the instability strip.
- The dominant pulsation frequency varies systematically across the instability strip, decreasing from $\sim$ 50–70 d^{-1} near the blue edge to $\sim$ 10–20 d^{-1} near the red edge, as expected from the scaling of acoustic frequencies with mean stellar density.
- The mean pulsation frequency, $\langle\nu_{\max}\rangle$, of δ Sct stars in open clusters correlates with cluster age, with $\log\langle\nu_{\mathrm{dom}}\rangle \propto a \log t$. This provides a new ensemble-asteroseismic age indicator that complements traditional isochrone-based methods.

Several avenues for future work follow directly. Spectroscopic follow-up of the slowly-rotating δ Sct pulsators will clarify whether these are physically distinct from the chemically peculiar Am stars that dominate the slow-rotator population in the same temperature range. The asymmetric mode splitting predicted by Z. Guo et al. (2024) provides a path towards mode identification in rapidly rotating δ Sct stars that should now be testable on the larger sample assembled here. Finally, the cluster mean-frequency–age relation invites extension to the older Gyr-scale clusters where δ Sct pulsators are rare, as well as replacement of $\langle\nu_{\rm max}\rangle$ with a per-star $\Delta\nu$, and a multi-cluster ensemble analysis that may simultaneously constrain age, metallicity, and helium abundance. The continued operation of *TESS* in faster cadence, together with the future delivery of *Gaia* DR4 astrometry and PLATO photometry (H. Rauer et al. 2025), will further improve our understanding of δ Sct variability.

ACKNOWLEDGMENTS

DRH acknowledges support from TESS GI programs 80NSSC24K0506, 80NSSC25K7910, and NASA ADAP 80NSSC24K0621. SJM was supported by the Australian Research Council through Future Fellowship FT210100485. TRB and PM were supported by the Australian Research Council through Laureate Fellowship FL220100117. D.H. and I.B. acknowledge support from the National Aeronautics and Space Administration (80NSSC25K7155). MK acknowledges The Kavli Foundation for their financial support in the framework of the Kavli Scholarship given to MK from 25/9/2023–30/9/2026. HK acknowledges support from National Science Foundation (NSF) Research Experience for Undergraduates (REU) Grant No. 2548017. This paper includes data collected with the TESS mission, obtained from the MAST data archive at the Space Telescope Science Institute (STScI). Funding for US Institutions for the TESS mission is provided by the NASA Explorer Program. STScI is operated by the Association of Universities for Research in Astronomy, Inc., under NASA contract NAS 5–26555. This work has made use of data from the European Space Agency (ESA) mission *Gaia* (https://www.cosmos.esa.int/gaia), processed by the *Gaia* Data Processing and Analysis Consortium (DPAC).

The playlist made while writing this paper can be found here.

Facilities: TESS, Gaia

Software: astropy (Astropy Collaboration et al. 2013), numpy (C. R. Harris et al. 2020), scipy (P. Virtanen et al. 2020), matplotlib (J. D. Hunter 2007), lightkurve (G. Barentsen et al. 2019), isoclassify (D. Huber et al. 2017), mwdust (J. Bovy et al. 2016a), TGLC (T. Han & T. D. Brandt 2023)

APPENDIX

A. DE-REDDENING GAIA PHOTOMETRY

The `isoclassify` posteriors provide line of sight extinction in the V band, whereas our formulation of absolute magnitude requires extinction in the *Gaia* G band. The *Gaia* passbands are broad enough that the ratio $k_X \equiv A_X/A_V$ is not a constant but rather depends on both the total extinction and on the intrinsic spectral energy distribution of the star, which, for our purposes is parametrised by the intrinsic color $(G_{\rm BP} - G_{\rm RP})_0$.

Over the color and extinction range spanned by our sample, k_G varies between 0.84 and 0.97, so we can not adopt a single fixed coefficient, which would bias A_G by up to 0.06 mag. We therefore adopt the coefficients tabulated by K. L. Luhman & T. L. Esplin (2020) in their Table 8, who fit $k_{\rm G,BP,RP}$ as polynomials in A_V and $(G_{\rm BP} - G_{\rm RP})_0$. of the form

$$k_X = c_0 + c_1 x + c_2 A_V + c_3 x A_V + c_4 x^2 A_V + 5A_V^2 + c_6 x^3 + c_7 A_V^3 + c_8 x^2 A_V^2, \qquad x \equiv (G_{\rm BP} - G_{\rm RP})_0, \qquad \text{(A1)}$$

with separate coefficient $c_0 \ldots c_8$ for each band. These fits are calibrated against the optical–infrared extinction curve of E. F. Schlafly et al. (2016) evaluated at $x = 0$ which corresponds to $R_V \simeq 3.3$ rather than the usual $R_V = 3.1$.

Note that Eq. A1 is a function of the intrinsic color, which is also not directly observed. Instead, we solve for it through an iteration regime. Starting from the observed color,

$$x^{(n+1)} = (G_{\rm BP} - G_{\rm RP}) - \left[k_{\rm BP}\left(x^{(n)}, A_V\right) - k_{\rm RP}\left(x^{(n)}, A_V\right)\right] A_V, \qquad x^{(0)} = (G_{\rm BP} - G_{\rm RP}), \qquad \text{(A2)}$$

and re-evaluate the BP and RP coefficients at the current estimate of the intrinsic color at each step. We find that the iteration converges to better than 10^{-4} mag within six steps, however, for a large enough extinction, the fixed point can lie outside the range over which Eq. A1 is fitted and then the iteration diverges. We therefore restrict x to the fitted range at each step and require $-0.2 < G_{\rm BP} - G_{\rm RP} < 1.5$ in the final sample selection. This second requirement removes stars for which the `isoclassify` A_V posterior is too large to be consistent with an observed *Gaia* color.

Having converged on x, the extinction in the G band follows as $A_G = k_G(x, A_V)\, A_V$, and we take the statistical uncertainty on A_G to be $k_G \sigma_{A_V}$, with σ_{A_V} the width of the `isoclassify` A_V posterior.

REFERENCES

Aerts, C., Christensen-Dalsgaard, J., & Kurtz, D. W. 2010, Asteroseismology, Astronomy and Astrophysics Library (Springer Netherlands), doi: 10.1007/978-1-4020-5803-5

Aerts, C., & Tkachenko, A. 2024, Astronomy and Astrophysics, 692, R1, doi: 10.1051/0004-6361/202348575

Antoci, V., Cunha, M., Houdek, G., et al. 2014, The Astrophysical Journal, 796, 118, doi: 10.1088/0004-637X/796/2/118

Antoci, V., Cunha, M. S., Bowman, D. M., et al. 2019, Monthly Notices of the Royal Astronomical Society, 490, 4040, doi: 10.1093/mnras/stz2787

Asplund, M., Grevesse, N., Sauval, A. J., & Scott, P. 2009, Annual Review of Astronomy and Astrophysics, 47, 481, doi: 10.1146/annurev.astro.46.060407.145222

Astropy Collaboration, Robitaille, T. P., Tollerud, E. J., et al. 2013, Astropy: A Community Python Package for Astronomy, https://arxiv.org/abs/1307.6212

Balona, L. A. 2018, Monthly Notices of the Royal Astronomical Society, doi: 10/gdnb3w

Balona, L. A., Daszyńska-Daszkiewicz, J., & Pamyatnykh, A. A. 2015, Monthly Notices of the Royal Astronomical Society, 452, 3073, doi: 10.1093/mnras/stv1513

Balona, L. A., & Dziembowski, W. A. 2011, Monthly Notices of the Royal Astronomical Society, 417, 591, doi: 10.1111/j.1365-2966.2011.19301.x

Barac, N., Bedding, T. R., Murphy, S. J., & Hey, D. R. 2021, in Posters from the TESS Science Conference II (TSC2, 193

Barac, N., Bedding, T. R., Murphy, S. J., & Hey, D. R. 2022, Monthly Notices of the Royal Astronomical Society, 516, 2080, doi: 10.1093/mnras/stac2132

Barceló Forteza, S., Moya, A., Barrado, D., et al. 2020, Astronomy and Astrophysics, 638, A59, doi: 10.1051/0004-6361/201937262

Barentsen, G., Hedges, C., Vinícius, Z., et al. 2019, KeplerGO/Lightkurve: Lightkurve v1.1.1,, Zenodo doi: 10.5281/zenodo.3371790

Bedding, T. R., Murphy, S. J., Hey, D. R., et al. 2020, Nature, 581, 147, doi: 10.1038/s41586-020-2226-8

Bedding, T. R., Murphy, S. J., Crawford, C., et al. 2023, The Astrophysical Journal, 946, L10, doi: 10.3847/2041-8213/acc17a

Berger, T. A., Huber, D., van Saders, J. L., et al. 2020, The Astronomical Journal, 159, 280, doi: 10.3847/1538-3881/159/6/280

Berger, T. A., Schlieder, J. E., & Huber, D. 2026, The Astronomical Journal, 171, 23, doi: 10.3847/1538-3881/ae0e76

Berry, I., Huber, D., Li, Y., et al. 2025, The Astrophysical Journal, 995, 128, doi: 10.3847/1538-4357/ae18c6

Berry, I., Huber, D., Li, Y., et al. 2026, arXiv e-prints, arXiv:2608.07792, doi: 10.48550/arXiv.2608.07792

Beyer, A. C., & White, R. J. 2024, The Astrophysical Journal, 973, 28, doi: 10.3847/1538-4357/ad6b0d

Bossini, D., Vallenari, A., Bragaglia, A., et al. 2019, Astronomy and Astrophysics, 623, A108, doi: 10.1051/0004-6361/201834693

Bovy, J., Rix, H.-W., Green, G. M., Schlafly, E. F., & Finkbeiner, D. P. 2016a, The Astrophysical Journal, 818, 130, doi: 10.3847/0004-637X/818/2/130

Bovy, J., Rix, H.-W., Schlafly, E. F., et al. 2016b, The Astrophysical Journal, 823, 30, doi: 10.3847/0004-637X/823/1/30

Bowman, D. M., & Kurtz, D. W. 2018, Monthly Notices of the Royal Astronomical Society, 476, 3169, doi: 10.1093/mnras/sty449

Boyajian, T. S., McAlister, H. A., van Belle, G., et al. 2012a, The Astrophysical Journal, 746, 101, doi: 10.1088/0004-637X/746/1/101

Boyajian, T. S., von Braun, K., van Belle, G., et al. 2012b, The Astrophysical Journal, 757, 112, doi: 10.1088/0004-637X/757/2/112

Boyajian, T. S., von Braun, K., van Belle, G., et al. 2013, The Astrophysical Journal, 771, 40, doi: 10.1088/0004-637X/771/1/40

Breger, M. 1979, Publications of the Astronomical Society of the Pacific, 91, 5, doi: 10.1086/130433

Breger, M. 2000, 210, 3

Breger, M., Lenz, P., & Pamyatnykh, A. A. 2009, Monthly Notices of the Royal Astronomical Society, 396, 291, doi: 10.1111/j.1365-2966.2008.14330.x

Cantat-Gaudin, T., Anders, F., Castro-Ginard, A., et al. 2020, Astronomy and Astrophysics, 640, A1, doi: 10.1051/0004-6361/202038192

Casagrande, L., Ramírez, I., Meléndez, J., Bessell, M., & Asplund, M. 2010, Astronomy and Astrophysics, 512, A54, doi: 10.1051/0004-6361/200913204

Catelan, M., & Smith, H. A. 2015, Pulsating Stars

Chaplin, W. J., Kjeldsen, H., Christensen-Dalsgaard, J., et al. 2011, Science, 332, 213, doi: 10.1126/science.1201827

Choi, J., Dotter, A., Conroy, C., et al. 2016, The Astrophysical Journal, 823, 102, doi: 10.3847/0004-637X/823/2/102

Collaboration, G., Vallenari, A., Brown, A. G. A., et al. 2023, Astronomy and Astrophysics, 674, A1, doi: 10.1051/0004-6361/202243940

Cortes, C., & Vapnik, V. 1995, Machine Learning, 20, 273, doi: 10.1023/A:1022627411411

Cox, J. P., King, D. S., & Stellingwerf, R. F. 1972, The Astrophysical Journal, 171, 93, doi: 10.1086/151262

Cummings, J. D., Kalirai, J. S., Tremblay, P.-E., Ramirez-Ruiz, E., & Choi, J. 2018, The Astrophysical Journal, 866, 21, doi: 10.3847/1538-4357/aadfd6

Dholakia, S., Murphy, S. J., Huang, C. X., Venner, A., & Wright, D. 2024, A Catalog of Binary Stars from Phase Modulation in the First Four Years of TESS Mission Photometry, arXiv, doi: 10.48550/arXiv.2410.19729

Dileep, A., Joshi, S., Lata, S., et al. 2025, MNRAS, 538, 1747, doi: 10.1093/mnras/staf361

Dotter, A. 2016, The Astrophysical Journal Supplement Series, 222, 8, doi: 10.3847/0067-0049/222/1/8

Drimmel, R., Cabrera-Lavers, A., & López-Corredoira, M. 2003, Astronomy and Astrophysics, 409, 205, doi: 10.1051/0004-6361:20031070

Dupret, M. A., Grigahcène, A., Garrido, R., Gabriel, M., & Noel, A. 2004, 559, 408

Dürfeldt-Pedros, O., Antoci, V., Smalley, B., et al. 2024, Astronomy and Astrophysics, 690, A104, doi: 10.1051/0004-6361/202349076

Frémat, Y., Royer, F., Marchal, O., et al. 2023, Astronomy and Astrophysics, 674, A8, doi: 10.1051/0004-6361/202243809

García Hernández, A., Pascual-Granado, J., Lares-Martiz, M., et al. 2024, in IAU Symposium, Vol. 376, IAU Symposium, ed. R. de Grijs, P. A. Whitelock, & M. Catelan, 239–249, doi: 10.1017/S1743921323003368

Gatuam, A., Murphy, S. J., & Bedding, T. R. 2026, MNRAS, 545, staf2001, doi: 10.1093/mnras/staf2001

Gootkin, K., Hon, M., Huber, D., et al. 2024, A New Catalog of 100,000 Variable \emph{TESS} A-F Stars Reveals a Correlation Between δ Scuti Pulsator Fraction and Stellar Rotation, doi: 10.48550/arXiv.2405.19388

Graczyk, D., Konorski, P., Pietrzyński, G., et al. 2017, The Astrophysical Journal, 837, 7, doi: 10.3847/1538-4357/aa5d56

Green, G. M., Schlafly, E. F., Finkbeiner, D. P., et al. 2015, The Astrophysical Journal, 810, 25, doi: 10.1088/0004-637X/810/1/25

Guo, F., Bloom, J. S., Wang, X., et al. 2025, Astronomy and Astrophysics, 699, A115, doi: 10.1051/0004-6361/202554169

Guo, Z., Bedding, T. R., Pamyatnykh, A. A., et al. 2024, Monthly Notices of the Royal Astronomical Society, 535, 2927, doi: 10.1093/mnras/stae2423

Han, T., & Brandt, T. D. 2023, The Astronomical Journal, 165, 71, doi: 10.3847/1538-3881/acaaa7

Harris, C. R., Millman, K. J., van der Walt, S. J., et al. 2020, Nature, 585, 357, doi: 10.1038/s41586-020-2649-2

Hey, D., & Aerts, C. 2024, Astronomy and Astrophysics, 688, A93, doi: 10.1051/0004-6361/202450489

Hey, D. R., Holdsworth, D. L., Bedding, T. R., et al. 2019, Monthly Notices of the Royal Astronomical Society, 488, 18, doi: 10.1093/mnras/stz1633

Houdek, G. 2000, 210, 454

Huber, D., Zinn, J., Bojsen-Hansen, M., et al. 2017, The Astrophysical Journal, 844, 102, doi: 10.3847/1538-4357/aa75ca

Hunt, E. L., & Reffert, S. 2023, Astronomy & Astrophysics, 673, A114, doi: 10.1051/0004-6361/202346285

Hunter, J. D. 2007, Computing in Science Engineering, 9, 90, doi: 10.1109/MCSE.2007.55

IJspeert, L. W., Tkachenko, A., Johnston, C., & Aerts, C. 2024, Astronomy and Astrophysics, 691, A242, doi: 10.1051/0004-6361/202450507

Jayasinghe, T., Kochanek, C. S., Stanek, K. Z., et al. 2018, Monthly Notices of the Royal Astronomical Society, 477, 3145, doi: 10.1093/mnras/sty838

Jenkins, J. M., Twicken, J. D., Tenenbaum, P. G., et al. 2021, Bulletin of the American Astronomical Society, 53, 134.01. https://baas.aas.org/pub/2021n1i134p01

Jia, Q., Chen, X., Wang, S., et al. 2025, The Astrophysical Journal, 984, 89, doi: 10.3847/1538-4357/adc685

Kliapets, M., Huijse, P., Tkachenko, A., et al. 2025, Astronomy and Astrophysics, 703, A240, doi: 10.1051/0004-6361/202556079

Kraft, R. P. 1967, The Astrophysical Journal, 150, 551, doi: 10.1086/149359

Kurtz, D. 2022, Asteroseismology across the HR Diagram, arXiv, doi: 10.48550/arXiv.2201.11629

Kurtz, D. W., Matthews, J. M., Martinez, P., et al. 1989, Monthly Notices of the Royal Astronomical Society, 240, 881, doi: 10.1093/mnras/240.4.881

Lara, F. E., & Rieutord, M. 2011, Astronomy & Astrophysics, 533, A43, doi: 10.1051/0004-6361/201117252

Li, G., Aerts, C., Bedding, T. R., et al. 2024, A&A, 686, A142, doi: 10.1051/0004-6361/202348901

Lindegren, L. 2018, Re-normalising the Astrometric Chi-square in Gaia DR2, Technical Note GAIA-C3-TN-LU-LL-124-01, European Space Agency, Gaia Data Processing and Analysis Consortium. https://www.cosmos.esa.int/web/gaia/public-dpac-documents

Lomb, N. R. 1976, Astrophysics and Space Science, 39, 447, doi: 10.1007/BF00648343

Luhman, K. L., & Esplin, T. L. 2020, AJ, 160, 44, doi: 10.3847/1538-3881/ab9599

Mani, P., Bedding, T. R., Bernizzoni, M., Murphy, S. J., & Hey, D. 2025, Monthly Notices of the Royal Astronomical Society, 542, 2866, doi: 10.1093/mnras/staf1400

Marshall, D. J., Robin, A. C., Reylé, C., Schultheis, M., & Picaud, S. 2006, Astronomy and Astrophysics, 453, 635, doi: 10.1051/0004-6361:20053842

McNamara, D. H. 2011, 142, 110, doi: 10.1088/0004-6256/142/4/110

Mo, Y., Zong, W., Wang, X., et al. 2026, A&A, 710, A245, doi: 10.1051/0004-6361/202660002

Mordelet, F., & Vert, J.-P. 2010, arXiv e-prints, arXiv:1010.0772, doi: 10.48550/arXiv.1010.0772

Mowlavi, N., Holl, B., Lecoeur-Taïbi, I., et al. 2023, Astronomy & Astrophysics, 674, A16, doi: 10.1051/0004-6361/202245330

Murphy, S. J. 2015, Monthly Notices of the Royal Astronomical Society, 453, 2569, doi: 10.1093/mnras/stv1842

Murphy, S. J., Bedding, T. R., Gautam, A., Kerr, R. P., & Mani, P. 2024a, The δ Scuti Stars of the Cep–Her Complex. I: Pulsator Fraction, Rotation, Asteroseismic Large Spacings, and the $\nu_{\rm Max}$ Relation, arXiv, doi: 10.48550/arXiv.2409.13135

Murphy, S. J., Bedding, T. R., Gautam, A., Kerr, R. P., & Mani, P. 2024b, Monthly Notices of the Royal Astronomical Society, 534, 3022, doi: 10.1093/mnras/stae2226

Murphy, S. J., Bedding, T. R., White, T. R., et al. 2022, Monthly Notices of the Royal Astronomical Society, 511, 5718

Murphy, S. J., & Gautam, A. 2026, arXiv e-prints, arXiv:2607.22060, doi: 10.48550/arXiv.2607.22060

Murphy, S. J., Gautam, A., & Claytor, Z. R. 2026, MNRAS, 550, stag1237, doi: 10.1093/mnras/stag1237

Murphy, S. J., Hey, D., Van Reeth, T., & Bedding, T. R. 2019, Monthly Notices of the Royal Astronomical Society, 485, 2380, doi: 10.1093/mnras/stz590

Murphy, S. J., Shibahashi, H., & Kurtz, D. W. 2013, Monthly Notices of the Royal Astronomical Society, 430, 2986, doi: 10.1093/mnras/stt105

Mwanzia, D. M., Lata, S., Chen, W. P., et al. 2025, The Astrophysical Journal, 985, 26, doi: 10.3847/1538-4357/adc696

Ortega, D. P., Mirouh, G. M., Hernández, A. G., Yanes, J. C. S., & Forteza, S. B. 2023, Astronomy & Astrophysics, 675, A167, doi: 10.1051/0004-6361/202346323

Palakkatharappil, D. B., & Creevey, O. L. 2023, A&A, 674, A146, doi: 10.1051/0004-6361/202243624

Pedregosa, F., Varoquaux, G., Gramfort, A., et al. 2011, Journal of Machine Learning Research, 12, 2825

Prša, A., Kochoska, A., Conroy, K. E., et al. 2022, The Astrophysical Journal Supplement Series, 258, 16

Qin, M., Fu, J.-N., Zong, W., et al. 2026, The Astrophysical Journal, 1002, 81, doi: 10.3847/1538-4357/ae56e9

Rauer, H., Aerts, C., Cabrera, J., et al. 2025, Experimental Astronomy, 59, 26, doi: 10.1007/s10686-025-09985-9

Read, A. K., Bedding, T. R., Mani, P., et al. 2024, Monthly Notices of the Royal Astronomical Society, 528, 2464, doi: 10.1093/mnras/stae165

Ricker, G. R., Winn, J. N., Vanderspek, R., et al. 2015, Journal of Astronomical Telescopes, Instruments, and Systems, 1, 014003, doi: 10.1117/1.JATIS.1.1.014003

Rodríguez, E., Balona, L. A., López-González, M. J., et al. 2020, MNRAS, 491, 4345, doi: 10.1093/mnras/stz3143

Royer, F., Zorec, J., & Gómez, A. E. 2007, Astronomy & Astrophysics, 463, 671, doi: 10.1051/0004-6361:20065224

Scargle, J. D. 1982, The Astrophysical Journal, 263, 835, doi: 10.1086/160554

Schlafly, E. F., Meisner, A. M., Stutz, A. M., et al. 2016, The Astrophysical Journal, 821, 78, doi: 10.3847/0004-637X/821/2/78

Schwarz, G. 1978, The Annals of Statistics, 6, 461, doi: 10.1214/aos/1176344136

Shibahashi, H., & Murphy, S. J. 2018, arXiv e-prints, arXiv:1811.10205

Soares-Furtado, M., Kuenzi, R., McClure, R. L., et al. 2026, AJ, 172, 137, doi: 10.3847/1538-3881/ae877e

Stassun, K. G., Oelkers, R. J., Pepper, J., et al. 2018, The Astronomical Journal, 156, 102, doi: 10.3847/1538-3881/aad050

Suárez, J. C., Goupil, M. J., & Morel, P. 2006, Astronomy & Astrophysics, 449, 673, doi: 10.1051/0004-6361:20054181

Théado, S., & Vauclair, S. 2003a, The Astrophysical Journal, 587, 795, doi: 10.1086/368261

Théado, S., & Vauclair, S. 2003b, The Astrophysical Journal, 587, 784, doi: 10.1086/368260

Théado, S., Vauclair, S., Alecian, G., & LeBlanc, F. 2011, SF2A-2011: Proceedings of the Annual meeting of the French Society of Astronomy and Astrophysics, 253

Théado, S., Vauclair, S., & Cunha, M. S. 2005, Astronomy and Astrophysics, 443, 627, doi: 10.1051/0004-6361:20052933

Thomson-Paressant, K., Neiner, C., Labadie-Bartz, J., et al. 2025, Astronomy and Astrophysics, 704, A134, doi: 10.1051/0004-6361/202556757

Uytterhoeven, K., Moya, A., Grigahcène, A., et al. 2011, Astronomy and Astrophysics, 534, A125, doi: 10.1051/0004-6361/201117368

VanderPlas, J. T. 2018, The Astrophysical Journal Supplement Series, 236, 16, doi: 10.3847/1538-4365/aab766

Vanlaer, V. 2026, VincentVanlaer/StORM,

Virtanen, P., Gommers, R., Oliphant, T. E., et al. 2020, Nature Methods, 17, 261, doi: 10.1038/s41592-019-0686-2

von Zeipel, H. 1924, Monthly Notices of the Royal Astronomical Society, 84, 684, doi: 10.1093/mnras/84.9.684

Wang, J., Chen, X., Deng, L., Zhang, J., & Sun, W. 2025, The Astrophysical Journal, 978, 53, doi: 10.3847/1538-4357/ad93b3

White, T. R., Huber, D., Maestro, V., et al. 2013, Monthly Notices of the Royal Astronomical Society, 433, 1262, doi: 10.1093/mnras/stt802

White, T. R., Huber, D., Mann, A. W., et al. 2018, Monthly Notices of the Royal Astronomical Society, 477, 4403, doi: 10.1093/mnras/sty898

Zhou, A.-Y. 2023, A Catalog of 59 Thousand δ Scuti Stars and Dozen Discoveries of New Variables with TESS Data, arXiv, doi: 10.48550/arXiv.2301.08355

Zhou, A.-Y. 2025, Research Notes of the AAS, 9, 23, doi: 10.3847/2515-5172/adaf8c

Zhou, A.-Y. 2025, NewA, 114, 102297, doi: 10.1016/j.newast.2024.102297

Ziaali, E., Bedding, T. R., Murphy, S. J., Van Reeth, T., & Hey, D. R. 2019, Monthly Notices of the Royal Astronomical Society, 486, 4348, doi: 10.1093/mnras/stz1110

Zorec, J., & Royer, F. 2012, Astronomy and Astrophysics, 537, A120, doi: 10.1051/0004-6361/201117691